

# Novel approach to apply existing constitutive soil models to the modelling of interfaces

Patrick Staubach<sup>1</sup>  | Jan Macháček<sup>2</sup>  | Torsten Wichtmann<sup>3</sup> 

<sup>1</sup> Chair of Soil Mechanics, Foundation Engineering and Environmental Geotechnics, Ruhr Universität Bochum, Germany/Chair of Geotechnics, Bauhaus Universität Weimar, Weimar, Germany

<sup>2</sup> Institute of Geotechnics, Technische Universität Darmstadt, Germany/Chair of Soil Mechanics, Foundation Engineering and Environmental Geotechnics, Ruhr-Universität Bochum, Bochum, Germany

<sup>3</sup> Chair of Soil Mechanics, Foundation Engineering and Environmental Geotechnics, Ruhr-Universität Bochum, Bochum, Germany

## Correspondence

Patrick Staubach, Chair of Soil Mechanics, Foundation Engineering and Environmental Geotechnics, Ruhr Universität Bochum, Germany/Chair of Geotechnics, Bauhaus Universität Weimar, Weimar, Germany.  
Email: [patrick.staubach@uni-weimar.de](mailto:patrick.staubach@uni-weimar.de)

## Abstract

A novel scheme to apply constitutive (continuum) soil models to the mechanical modelling of soil-structure interfaces is presented. Opposite to existing approaches, all normal stress components of the interface depend directly on the normal stress components of the adjacent continuum. This allows to satisfy boundary conditions not only for the continuum but also for the interface. Interface models based on Hypoplasticity with intergranular strain extension and on Sanisand (version of 2004) are formulated. They are implemented in the framework of a mortar contact discretisation technique in a finite element code, which is available for download. A numerical differentiation scheme is used to secure consistent derivatives of contact forces with respect to displacement. The performance of the proposed interface models is evaluated by comparison with data from (cyclic) simple interface shear tests and an existing (hypoplastic) interface model proposed by Stutz et al. (2016). Subsequently, a large-scale cyclic interface shear test with complex geometry is simulated using the different interface models. It is concluded that only the novel interface formulation allows to appropriately consider the boundary conditions of the large-scale interface shear test in the interface.

## KEYWORDS

contact mechanics, friction, hypoplasticity, interface modelling, interface shear test, Sanisand

## 1 | INTRODUCTION

The modelling of soil-structure interfaces is an important aspect of numerical geomechanics. Great care has to be taken in the numerical treatment of the contact constraints since they add severe non-linearity to the problem at hand. This includes the discretisation of the contacts, the enforcement of the contact constraints and the constitutive description of the interface zone. For the modelling of pile driving processes or axial loading of piles in general, the adequate incorporation of frictional forces between pile and soil is a key point for the successful prediction of the overall process.<sup>1–5</sup> Since pile driving potentially involves cyclic interface shearing, the constitutive interface models have to be able to reproduce the soil response in loading and unloading processes, which is not realistically possible using a simple Coulomb friction model.<sup>6</sup>

This is an open access article under the terms of the [Creative Commons Attribution-NonCommercial](https://creativecommons.org/licenses/by-nc/4.0/) License, which permits use, distribution and reproduction in any medium, provided the original work is properly cited and is not used for commercial purposes.

© 2022 The Authors. *International Journal for Numerical and Analytical Methods in Geomechanics* published by John Wiley & Sons Ltd.

For the numerical modelling of the mechanical behaviour of the interface zone (i.e., the friction model), two general approaches exist. The employed constitutive models are either specifically tailored for the application to interfaces and are solely used as friction models (see e.g., the models presented in Ref. 7–19) or they are based on models originally developed for the constitutive modelling of the continuum (see e.g., Ref. 6, 20–27). For the second approach, the stress and strain in the interface have to be given in a global continuum setting (i.e., the full tensors), whereas in the first approach only the normal (contact) stress, the shear stress and the shear strain of the interface zone are conventionally considered. Using the second approach, a slight modification of the constitutive equations of the continuum model is often necessary to account for the characteristics of the soil-structure interface, such as the surface roughness. Compared to the first approach, the application of existing continuum models to the modelling of interfaces has the advantage that the constitutive model needs not to be formulated completely new<sup>1,20,21,28</sup>. Moreover, apart from the surface roughness and the shear band thickness, no additional constitutive parameters are usually required for the friction model since they are typically identical to those used for the continuum constitutive model. Therefore, additional interface shear tests to calibrate the parameters of the friction model are not required in all cases.

The existing approaches for the direct application of continuum models to the interface have different shortcomings, which are discussed by Stutz et al.<sup>23,26</sup> The more recently presented approach by Stutz et al. is more promising, because it is possible to consider the normal strain of the interface, which has been neglected in earlier schemes. In addition, differing normal stress components can be taken into account. However, as will be shown in this work, the approach by Stutz et al. can violate the boundary conditions of a system, caused by un-realistic (initial) jumps in the normal stress components in the transition zone between interface and continuum. To overcome this shortcoming, a new interface formulation is presented, taking into account the stress acting in the continuum adjacent to the interface. Using the novel interface formulation, a hypoplastic interface model with intergranular strain extension<sup>29,30</sup> and a Sanisand<sup>31</sup> interface model are presented. In addition, a numerical differentiation scheme is introduced, securing consistent derivatives of contact forces with respect to displacement, in order to achieve good convergence behaviour in the implicit solving scheme despite the strong non-linearity added by the complex interface models. Finally, the numerical robustness of the proposed approaches and applicability to boundary value problems (BVPs) is demonstrated by the back-analysis of large-scale cyclic interface shear tests.

## 2 | GENERAL AND CONTACT MECHANICS NOTATION

The following general notation is used: Vectors and second order tensors are written with bold font, for example,  $\mathbf{a}$  and  $\mathbf{A}$ . A Cartesian coordinate system with the orthogonal unit vectors  $\mathbf{e}_i$  for  $i = 1, 2, 3$  is used. This system may be subjected to a rotation then given by unit vectors  $\mathbf{e}'_i$  (still orthogonal). Einstein's summation convention is used. Fourth order tensor are written sans serif, for example,  $\mathbf{E}$ . For the vector product  $(\cdot)$ ,  $\mathbf{a} \cdot \mathbf{b} = a_i b_i$  holds. The trace of a tensor is  $\text{tr}(\mathbf{A}) = A_{ii}$ . Contraction of tensors is written with a colon for second order tensors  $\mathbf{A} : \mathbf{B} = \text{tr}(\mathbf{A} \cdot \mathbf{B}^T) = A_{ij} B_{ij}$ . Dyadic multiplication is written  $\mathbf{A} \otimes \mathbf{A} = A_{ij} A_{kl}$ . The euclidean norm  $\|\mathbf{A}\| = \sqrt{\mathbf{A} : \mathbf{A}}$  is used. Furthermore,  $\mathbf{I} = \text{diag}[1, 1, 1] = \{[1, 0, 0]^T, [0, 1, 0]^T, [0, 0, 1]^T\}$  and  $\mathbf{0} = [0, 0, 0]^T$  are defined. If not stated otherwise, the mechanical sign convention for (continuum) stress  $\boldsymbol{\sigma}$  and strain  $\boldsymbol{\varepsilon}$  is used. Classically, one surface of the contact pair is denoted as the slave ( $\sqcup^{(1)}$ ) and the other as master ( $\sqcup^{(2)}$ ) surface. The surface traction is defined by

$$\mathbf{t} = \boldsymbol{\sigma} \cdot \mathbf{n}^{(1)}, \quad (1)$$

wherein  $\mathbf{n}^{(1)}$  is the normal vector of the slave surface and  $\boldsymbol{\sigma}$  is the stress tensor. The normal vector of the master surface  $\mathbf{n}^{(2)}$  is given by

$$\mathbf{n}^{(2)} = -\mathbf{n}^{(1)}. \quad (2)$$

The contact stress of the contact pair can be separated in its normal and tangential component, viz.

$$\mathbf{t} = \mathbf{t}_N + \mathbf{t}_T. \quad (3)$$

The normal stress component  $t_N$  and the normal stress vector  $\mathbf{t}_N$  are

$$t_N = -\mathbf{n}^{(2)} \cdot \boldsymbol{\sigma} \cdot \mathbf{n}^{(1)} \quad \text{and} \quad \mathbf{t}_N = -\mathbf{n}^{(2)} t_N. \quad (4)$$

The tangential stress vector is defined by

$$\mathbf{t}_T = \mathbf{t} - \mathbf{t}_N = (\mathbf{I} - \mathbf{n}^{(2)} \otimes \mathbf{n}^{(2)}) \cdot \mathbf{t}. \quad (5)$$

The minimum distance between slave and master surface is evaluated by the euclidean norm

$$\mathbf{x}^{(2)}(\mathbf{x}^{(1)}) = \arg(\min \|\mathbf{x}^{(1)} - \mathbf{x}^{(2)}\|), \quad (6)$$

where  $\mathbf{x}$  is the spatial coordinate in the current configuration. The gap is calculated using

$$\mathbf{g} = \mathbf{X}^{(1)} + \mathbf{u}^{(1)} - (\mathbf{X}^{(2)} + \mathbf{u}^{(2)}) = \mathbf{g}_0 + \mathbf{u}^{(1)} - \mathbf{u}^{(2)}, \quad (7)$$

where  $\mathbf{g}_0$  is the gap in the reference configuration and  $\mathbf{u}$  the displacement.  $\mathbf{X}$  is the spatial coordinate in the reference configuration. Similar to the contact stress, the contact gap has a normal

$$\mathbf{g}_N = \mathbf{n}^{(2)} \otimes \mathbf{n}^{(2)} \cdot \mathbf{g} \quad (8)$$

and a tangential part

$$\mathbf{g}_T = (\mathbf{I} - \mathbf{n}^{(2)} \otimes \mathbf{n}^{(2)}) \cdot \mathbf{g}. \quad (9)$$

More details on the enforcement of the contact conditions as well as on the applied (element-based) mortar contact discretisation technique<sup>32–34</sup> can be found in Appendix A. All numerical schemes presented in the following are implemented in the finite element code numgeo<sup>2</sup>.

### 3 | ADVANCED CONSTITUTIVE INTERFACE MODELS FOR SAND

#### 3.1 | Interface behaviour of sands

The mechanical behaviour of sand-structure interfaces is strongly influenced by the surface roughness  $\kappa$ . For relatively smooth surfaces the contact friction angle is often fully mobilised after a short shear path and remains almost constant after mobilisation.<sup>43</sup> For rough surfaces; however, the behaviour is similar to the response observed in simple shear or triaxial tests performed on dense sand, where the peak stress is followed by gradual softening with ongoing shearing. Compared to smooth surfaces, the shear band is usually much broader for rough surfaces. These characteristics of the constitutive interface behaviour of sand are schematically shown in Figure 1A.

Interface shear tests are performed to determine the mechanical properties of soil-structure interfaces and can, amongst other criteria, categorised according to their boundary conditions. Figure 1B displays schematics of simple interface shear tests with constant normal stiffness ( $K$  constant, CNS test) and constant normal load ( $t_N$  constant, CNL test). For most BVPs, constant normal stiffness conditions are believed to be more representative, since the shearing of the interface leads to volumetric strain and hence change in the normal contact stress. The influence of the constant normal stiffness and constant normal load boundary conditions on the shear stress versus tangential displacement curves is also schematically shown in Figure 1B. CNS tests do not exhibit a peak in the  $t_T$  versus  $u_T$  plot and reach higher maximum shear stress with increasing normal stiffness. In case of CNL tests, the curves show a peak while higher normal load results in a higher maximum shear stress. Larger relative displacements between the soil sample and the structure are necessary in case of higher normal load to reach the peak value of  $t_T$  compared to lower normal load.<sup>44</sup>

The aforementioned characteristics of the constitutive behaviour of sand-structure interfaces are confirmed by numerous monotonic (see e.g., Ref. 45–49) and cyclic interface shear tests (see e.g., Ref. 50–53) reported in the literature. In addition, these characteristics have also been reproduced using the discrete element method.<sup>54–56</sup>

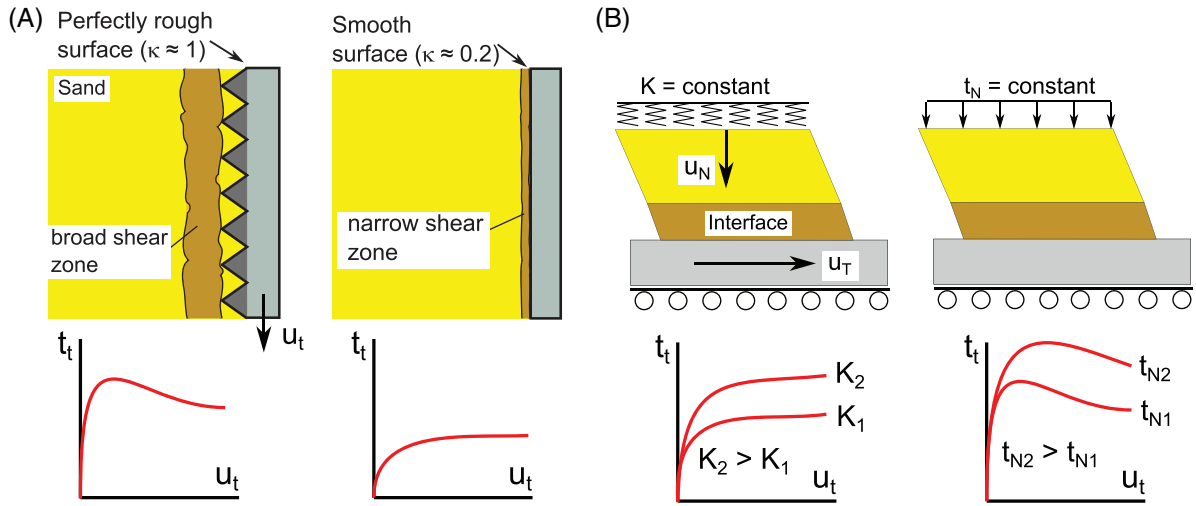


**FIGURE 1** (A) Schematic of the shear stress versus tangential displacement response of soil-structure interfaces in dependence of the surface roughness (based on Ref. 43). (B) Different boundary conditions used in simple interface shear tests and their influence on the shear stress versus tangential displacement response

### 3.2 | Modelling of interfaces using existing constitutive continuum models

As is visible from the  $t_T$  versus  $u_T$  curves in Figure 1, the constitutive behaviour of the interface zone is more complex than can be modelled using a simple elasto-plastic model such as the Coulomb friction. Hence, several researchers have developed advanced constitutive contact models, which are able to account for the influence of relative density, for the stress state in the interface as well as for the loading history. Herle & Nübel,<sup>57</sup> Gutjahr<sup>20</sup>, and Arnold & Herle<sup>21,28</sup> were among the first to apply hypoplastic continuum models to the modelling of interfaces. They modified the hypoplastic relations such that they are applicable for plane conditions (Herle & Nübel, Gutjahr) or assumed identical normal stress components<sup>3</sup>  $\sigma_{11}^{\text{interface}} = \sigma_{22}^{\text{interface}} = \sigma_{33}^{\text{interface}}$  (Arnold & Herle) in the hypoplastic interface element. Stutz et al.<sup>6,23–26</sup> later enhanced the approach by Arnold & Herle, allowing for non-identical normal stress components in the interface element.

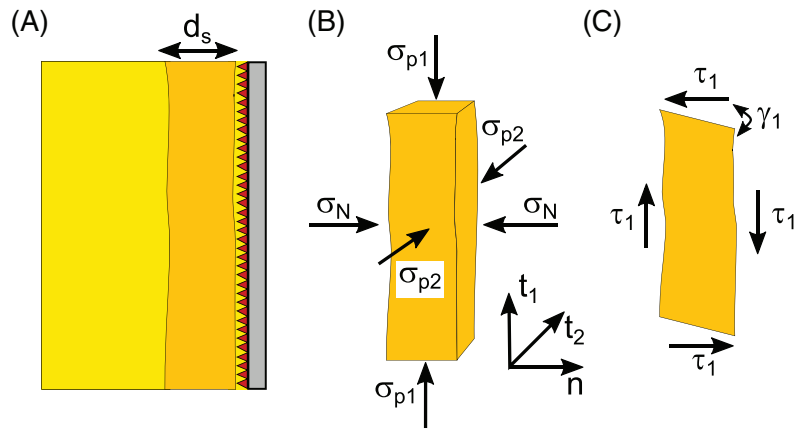
Apart from the application of (existing) constitutive continuum models, several stand-alone constitutive interface models have been proposed (see Ref. 7, 9–13, 15, 16, 22, 27), which are all based on an additive split of elastic and plastic strains (i.e., elasto-plastic models). These models are of "Coulomb"-type with respect to the stress conditions in the interface, that is, only normal and shear stress but no in-plane interface normal stress components are considered. Therefore, the interface shear stress rate is a function of the interface normal stress  $\sigma_N$  (identical to the normal contact stress  $t_N$ ) and potentially some other state variables  $\mathbf{k}$  (including the shear stress  $\tau$ ), that is,  $\dot{\tau} = f(\sigma_N, \mathbf{k})$ .

A general framework to apply existing constitutive continuum models as constitutive interface models is presented in the following. For this purpose, the approach by Stutz et al. is enhanced such that the normal stress components in the interface are directly dependent on the stress of the adjacent continuum, allowing to satisfy the boundary conditions of a BVP in the interface.

### 3.3 | Stress and strain conditions in the interface element

The interface element is formulated as zero-thickness element, so that no remeshing of discrete interface elements is required to simulate large relative tangential displacements. Figure 2 displays a schematic of a shear band with thickness  $d_s$  (Figure 2A), the normal stress components acting in the shear band including the local coordinate system of the interface (Figure 2B) and an idealised interface element in 2D subjected to the shear strain  $\gamma_1$ . The local coordinate system of the interface has the basis vector  $\mathbf{n}$  for the normal direction and the two tangential basis vectors  $\mathbf{t}_1$  and  $\mathbf{t}_2$ . The components of the normal stress of the interface element are likewise defined by  $\sigma_n$  for the normal and  $\sigma_{p1}$ ,  $\sigma_{p2}$  for the normal stress components in-plane. The interface element is further subjected to the two shear stress components  $\tau_1$  and  $\tau_2$  acting in the  $\mathbf{n} - \mathbf{t}_1$  and  $\mathbf{n} - \mathbf{t}_2$  plane, respectively.

FIGURE 2 (A) Shear band with thickness  $d_s$  formed at a soil-structure interface. (B) Normal stress components acting in the shear band. (C) Shear strain and stress in a 2D interface element



In the approach by Stutz et al.,<sup>26</sup> the following definitions of stress and strain tensors are used for the constitutive continuum model applied as interface model

$$\boldsymbol{\sigma}^{\text{interface}} = \begin{bmatrix} \sigma_N & \tau_1 & \tau_2 \\ \tau_1 & \sigma_{p1} & 0 \\ \tau_2 & 0 & \sigma_{p1} \end{bmatrix} \quad \text{and} \quad \boldsymbol{\varepsilon}^{\text{interface}} = \begin{bmatrix} \varepsilon_N & \gamma_1/2 & \gamma_2/2 \\ \gamma_1/2 & 0 & 0 \\ \gamma_2/2 & 0 & 0 \end{bmatrix}. \quad (10)$$

In contrast to the approaches by Gutjahr and Arnold & Herle, the normal strain  $\varepsilon_N$  of the interface is considered. To determine  $\varepsilon_N$ , the increment of normal contact stress  $\Delta t_N$  is enforced to be identical to the stress increment in normal direction of the interface  $\Delta\sigma_N$  computed using the constitutive continuum model equations, viz.

$$\Delta\sigma_N - \Delta t_N \stackrel{!}{=} 0. \quad (11)$$

Therein,  $\stackrel{!}{=}$  symbolises that Equation (11) has to be enforced. Equation (11) is solved using a Newton iteration in form of

$$\Delta\varepsilon_N^{n+1} = \Delta\varepsilon_N^n - (\Delta\sigma_N^n - \Delta t_N^n) / \frac{\partial \Delta\sigma_N^n}{\partial \Delta\varepsilon_N^n}. \quad (12)$$

The iteration is performed  $n$ -times until the left-hand side of Equation (11) is sufficiently close to zero.

Since for most constitutive soil models  $\frac{\partial \Delta\sigma_{ii}}{\partial \Delta\varepsilon_{11}} \neq 0_{ii}$  applies, the interface normal stress components  $\sigma_{p1}$  and  $\sigma_{p2}$  change with  $\Delta\varepsilon_N$ . In the same way the intergranular strain tensor, representing an important state variable of the hypoplastic model with intergranular strain extension, changes with  $\Delta\varepsilon_N$  as well as with the shear strain increment  $\Delta\boldsymbol{\gamma}$ .

It is important to note that the constitutive response is influenced by the normal contact stress history since the normal stress components of the continuum model develop with increasing normal contact stress. Therefore, the contact behaviour should be described in all steps with the same constitutive contact model when applying the approach by Stutz et al. In the implementation by Stutz et al., the assumption  $\sigma_{p1} = \sigma_{p2}$  is made (see Equation (10)). Due to restrictions of the closed-source software Abaqus used by Stutz et al. for the implementation of the interface model, the initial normal stress components furthermore have to be set isotropically, that is,  $\sigma_{p1,0} = \sigma_{p2,0} = \sigma_{N,0}$ .<sup>25</sup>

Using the approach by Stutz et al., a *jump* in the stress tensor between continuum and interface generally exists. The following condition of the jump  $[[\boldsymbol{\sigma}]] = \boldsymbol{\sigma}^{\text{interface}} - \boldsymbol{\sigma}^{\text{continuum}}$  has to be satisfied<sup>58,59</sup>:

$$[[\boldsymbol{\sigma}]] \cdot \mathbf{n} = \mathbf{0}. \quad (13)$$

For plain-strain conditions, only one jump in the stress acting parallel to the discontinuity line ( $\sigma_{p1}$ ) is permitted (the other in-plane stress component ( $\sigma_{p2}$ ) is not governed by Equation (13), but of course a jump is possible). For 3D, three jumps at the discontinuity plane are allowed by static considerations, which are the normal stress components  $\sigma_{p1}$  and  $\sigma_{p2}$  given in Figure 2 as well as the shear stress component in the  $\mathbf{t}_1 - \mathbf{t}_2$  plane.

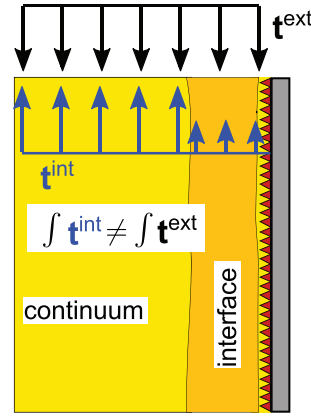


FIGURE 3 Illustration of the jump in the internal vertical stress vector  $\mathbf{t}^{int}$  between continuum and interface in case of an external load ( $\mathbf{t}^{ext}$ )

Using the approach by Stutz et al., both normal stress components orientated tangentially to the discontinuity plane may jump. This is allowed according to Equation (13) but is not necessarily realistic. The approach by Stutz et al. can violate the boundary conditions of a BVP. For instance, if a prescribed traction parallel to a discontinuity line exists, the corresponding stress component in the interface is not necessarily identical to it. Such a case is illustrated in Figure 3. Even though a vertical traction is prescribed, the vertical stress in the interface zone is only governed by the interface strain in normal direction, which does in general not lead to a vertical stress in the interface being in equilibrium with the prescribed external loading. The developing normal interface stress components depend, among other influencing factors, on the lateral stress coefficient. Moreover, using the approach by Stutz et al, no strain of the interface zone in direction of the vertical traction can be taken into account. This is a major disadvantage, considering that the hypoplastic model with intergranular strain extension is considerably influenced by the strain history. In addition, a jump already exists prior to shearing and the initial stress conditions might not be correctly reflected. In summary, the approach by Stutz et al. has the following shortcomings:

- The stress state in the interface is not directly governed by the boundary conditions
- An (initial) jump in the stress tensor between continuum and interface generally exists
- The in-plane normal strain components in the interface are not accounted for

In order to address the shortcomings of the approach by Stutz et al., the stress tensor of the adjacent continuum is extrapolated to the interface element, avoiding the (initial) jump in the stress and the violation of boundary conditions. The extrapolation of the stress tensor from the integration points of the adjacent continuum elements to the surface nodes is performed by

$$\boldsymbol{\sigma}^{extra} = \sum_{igp}^{ngp} N_{igp}(\xi', \eta') \boldsymbol{\sigma}_{igp}^{continuum}, \quad (14)$$

where  $\xi'$  and  $\eta'$  are the stretched local coordinates (see Figure 4B) of the adjacent continuum element from which the stress is retrieved.  $\boldsymbol{\sigma}^{extra}$  is the extrapolated stress given in the global coordinate system and  $\boldsymbol{\sigma}_{igp}^{continuum}$  is the stress in integration point  $igp$  of the adjacent continuum element.  $ngp$  is the number of all integration points of the considered continuum element. Note that if the point on the interface lies exactly between two or more continuum elements, the average values of the extrapolated stresses of all adjacent elements are computed. The stress has to be rotated according to the local coordinate system of the interface element. The rotation is defined by

$$\boldsymbol{\sigma}'^{extra} = \boldsymbol{\alpha} \cdot \boldsymbol{\sigma}^{extra} \cdot \boldsymbol{\alpha}^T, \quad (15)$$

where

$$\alpha_{ij} = \mathbf{e}'^{(i)} \cdot \mathbf{e}^{(j)}. \quad (16)$$

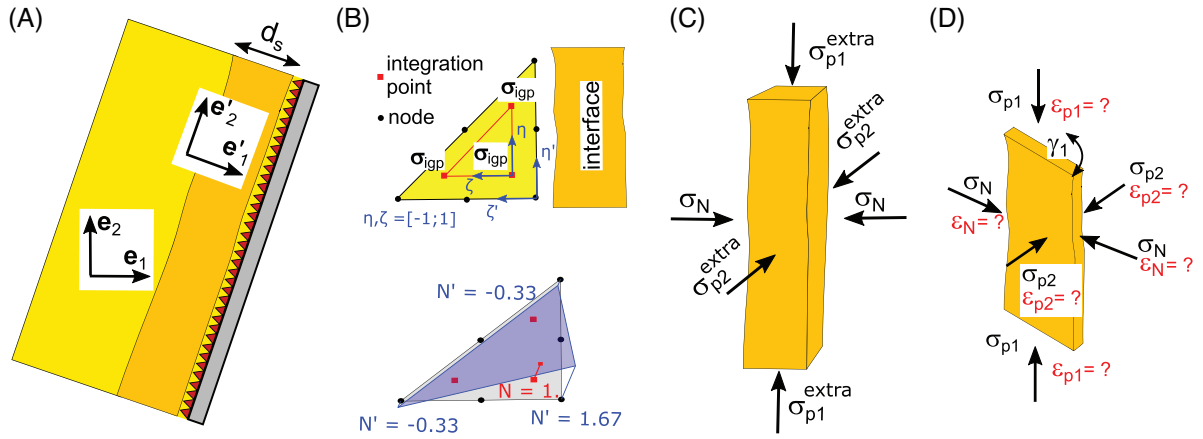


**FIGURE 4** (A) Global and local coordinate system of the interface. (B) Extrapolation of the continuum stress to the interface. (C) Normal stress components acting in the interface. (D) Boundary conditions of the novel interface element formulation

$\mathbf{e}'^{(i)}$  is the  $i$ -th basis vector of the local interface coordinate system and  $\mathbf{e}^{(j)}$  is the  $j$ -th basis vector of the global coordinate system. The rotation from global to local coordinate system is displayed in Figure 4A. Only the interface normal stress components  $\sigma_{p1}^{extra}$  and  $\sigma_{p2}^{extra}$  of  $\boldsymbol{\sigma}'^{extra}$  are of interest. The other components of the stress tensor ( $\sigma_N$ ,  $\tau_1$ ,  $\tau_2$ ) are obtained using the contact stress vector  $\mathbf{t}$  of the previous converged state (this is either the solution at the last global iteration or the solution at the last converged sub-increment, as is further explained in Section 3.5). The stress components of the interface element using the extrapolated stress are given in Figure 4C. Using the proposed definitions for the stress state of the interface element, Equation (10) is modified to Equation (17):

$$\bar{\boldsymbol{\sigma}}^{interface} = \begin{bmatrix} \sigma_N & \tau_1 & \tau_2 \\ \tau_1 & \sigma_{p1} & 0 \\ \tau_2 & 0 & \sigma_{p2} \end{bmatrix} \quad \text{and} \quad \bar{\boldsymbol{\epsilon}}^{interface} = \begin{bmatrix} \epsilon_N & \gamma_1/2 & \gamma_2/2 \\ \gamma_1/2 & \epsilon_{p1} & 0 \\ \gamma_2/2 & 0 & \epsilon_{p2} \end{bmatrix} \quad (17)$$

Note that the assumption of  $\sigma_{p1} = \sigma_{p2}$  is neither required nor made. In addition, the strains  $\epsilon_{p1}$  and  $\epsilon_{p2}$  are not necessarily zero as assumed by Stutz et al, which is also indicated in Figure 4D. For 2D plain-strain analyses, however, the normal strain component  $\epsilon_{p2}$  is zero of course. Changes of normal strain components  $\epsilon_{p1}$  and  $\epsilon_{p2}$  are only driven by a change in the continuum stress field, which modifies normal stress in the interface ( $\sigma_{p1}$  and  $\sigma_{p2}$ ). If pure shearing of the interface occurs, the approach reduces to the approach by Stutz et al. in terms of the strain tensor ( $\epsilon_{p1} = \epsilon_{p2} = 0$ ). An example for such conditions is given later with the simulation of simple interface shear tests.

Note that the second approach presented by Ref. 22 also considers all stress components similar to Equation (17). However, in analogy to the approach by Stutz et al., the stress is also not directly influenced by the adjacent continuum stress.

The contact normal stress  $t_N$  and the extrapolated (rotated) stress components ( $\sigma_{p1}^{extra}$  and  $\sigma_{p2}^{extra}$ ) have to be in equilibrium with the stress of the interface element. This is enforced by

$$\sigma_N - t_N \stackrel{!}{=} 0, \quad (18)$$

$$\sigma_{p1} - \sigma_{p1}^{extra} \stackrel{!}{=} 0 \quad \text{and} \quad (19)$$

$$\sigma_{p2} - \sigma_{p2}^{extra} \stackrel{!}{=} 0. \quad (20)$$

Note that the shear stress components of the continuum need not to be enforced to be in equilibrium with the contact shear stresses since they are identical by definition. Note in addition that Equations (18 - 20) are not formulated incrementally since stress equilibrium is enforced. According to the jump condition given by Equation (13), Equations (19 - 20) need not necessarily be satisfied. They can be enforced according to the boundary conditions of the considered BVP. In general, however, Equations (18 - 20) should be satisfied initially (prior to shearing) if homogeneity is assumed.

Using the Jacobian  $\mathbf{J}$  of the constitutive continuum model applied as interface model, Equations (18 - 20) are solved using Newton's method with iterative calculation of the unknown strain, viz.

$$\boldsymbol{\varepsilon}^{\text{interface},n+1} = \boldsymbol{\varepsilon}^{\text{interface},n} - \mathbf{J}^{-1} : \left( \boldsymbol{\sigma}^{\text{interface}} - \boldsymbol{\sigma}'^{\text{extra}} \right), \quad (21)$$

where  $\boldsymbol{\sigma}'^{\text{extra}} = \text{diag}[t_N, \sigma_{p1}^{\text{extra}}, \sigma_{p2}^{\text{extra}}]$  and  $\boldsymbol{\sigma}^{\text{interface}} = \text{diag}[\sigma_N, \sigma_{p1}, \sigma_{p2}]$ . Equation (21) is solved in two steps. First,

$$\mathbf{J}\Delta\boldsymbol{\varepsilon}^{\text{interface},n} = -\left( \boldsymbol{\sigma}^{\text{interface}} - \boldsymbol{\sigma}'^{\text{extra}} \right) \quad (22)$$

is solved for  $\Delta\boldsymbol{\varepsilon}^{\text{interface},n} = \boldsymbol{\varepsilon}^{\text{interface},n+1} - \boldsymbol{\varepsilon}^{\text{interface},n}$  and then added to the total strain of iteration  $n$ , viz.

$$\boldsymbol{\varepsilon}^{\text{interface},n+1} = \boldsymbol{\varepsilon}^{\text{interface},n} + \Delta\boldsymbol{\varepsilon}^{\text{interface},n}. \quad (23)$$

In each iteration  $n$ , the shear stress components of the contact stress vector  $\mathbf{t}$  from the last converged state are added to  $\boldsymbol{\sigma}^{\text{interface}}$

$$\bar{\boldsymbol{\sigma}}^{\text{interface}} = \boldsymbol{\sigma}^{\text{interface}} + \mathbf{T}, \quad (24)$$

where  $\mathbf{T} = \{[0, \tau_1, \tau_2]^T, [\tau_1, 0, 0]^T, [\tau_2, 0, 0]^T\}$ . This is done because only the normal stress components are supposed to change during the iterative calculation of the increments of the normal strain components. During the update of the normal strains, the shear stresses are not considered in Equation (22) but the constitutive model is called using  $\bar{\boldsymbol{\sigma}}^{\text{interface}}$ , including the shear stress components from the last converged iteration. Since the increment in shear strain is non-zero, the shear stress components change during the Newton iteration. The contact shear stress vector  $\mathbf{t}_T$  is, however, only updated in case Equations (18 - 20) are satisfied. The definition of the shear strain components in  $\bar{\boldsymbol{\varepsilon}}^{\text{interface}}$  is given in the next Section.

### 3.4 | Shear strain

Using zero-thickness interface elements, the increment in shear strain is calculated by

$$\tan \Delta\gamma = \frac{\Delta\mathbf{g}_T}{d_s}, \quad (25)$$

where the interface thickness  $d_s$  and the increment in tangential gap  $\Delta\mathbf{g}_T$  (see Equation (A13)) are used. For granular media, the interface thickness is usually assumed identical to the shear band thickness, which is a function of the grain size for cohesion-less soils. According to laboratory observations,<sup>10,47,60,61</sup> the shear band developing at soil-structure interfaces during shearing has a thickness of approximately  $5 - 10 \cdot d_{50}$ , where  $d_{50}$  is the median grain size. It is important to note that the shear band thickness is usually not constant with respect to shear strain.<sup>62</sup> The definitions of the strain conditions in the interface element introduced in Section 3.3 allow to consider the change of the interface thickness with respect to the normal strain and hence enable to consider the dilatancy of the interface zone. The interface thickness is calculated by

$$d_s = d_{s0} + \varepsilon_N \cdot d_{s0}, \quad (26)$$

where  $d_{s0}$  is the initial interface thickness, estimated using the aforementioned approximation based on experimental results. Note that the influence of the consideration of the change in shear band thickness on the calculated shear strain is not large. For the simulations presented later the normal strain did not exceed 10 % in most cases, leading to comparably small changes in  $d_s$ . Note in addition that even though the shear band thickness introduces a parameter which is hard to estimate and may involve a great uncertainty, using a Coulomb friction model also requires the definition of a tangential penalty factor (or a relative tangential displacement at which the shear stress is fully mobilised as e.g., implemented in the commercial software Abaqus<sup>63</sup>). This parameter is equivalently hard to estimate as is estimating  $d_s$ .

In analogy to Equation (24), the shear components of the strain tensor are added to  $\bar{\epsilon}^{\text{interface}}$  in every iteration  $n$ , viz.

$$\bar{\epsilon}^{\text{interface}} = \epsilon^{\text{interface}} + \mathbf{E}, \quad (27)$$

where  $\mathbf{E} = \{[0, \gamma_1/2, \gamma_2/2]^T, [\gamma_1/2, 0, 0]^T, [\gamma_2/2, 0, 0]^T\}$ .

### 3.5 | Implementation

The pseudocode of the implementation is given in Algorithm 1. An explicit sub-increment scheme with error control is applied, for which the shear strain increment is divided in  $n_{\text{sub}}$  sub-increments in line 1. A fixed maximum sub-increment of  $5 \cdot 10^{-6}$  for the increment in shear strain is used. During the Newton iteration, the strain increment is calculated using Equation (27) with the sub-increment of shear strain and the increments of the normal strain components from the last iteration. The sub-increment of shear strain is constant. In each iteration, the state variables  $\mathbf{k}$  of the constitutive interface model and the full stress tensor are first set to the values of the previous converged sub-increment in lines 5 and 6. The constitutive continuum model updates the stress and the state variables in line 7 based on the strain increment  $\Delta \bar{\epsilon}^{\text{interface},i}$ . Using the updated stress tensor, the updated normal strain increment is calculated in line 8. Lastly, the error  $r$  is calculated using Equations (18 - 20). The tolerance  $tol$  for the error is chosen as  $tol = 0.2\%$ , which originates from experience when integrating the stress rate of the hypoplastic model. The state variables and the updated stress tensor are saved after convergence in lines 11 and 12. Note that the algorithm is independent of the underlying constitutive continuum model applied.

Depending on the constitutive model used, the iterative procedure can be computationally expensive. The evaluation of the contact contributions implemented in `numgeo` can be performed in parallel using multiple threads. Since the required communication of the threads is little compared to the time spent in the update of the contact contributions, an almost linear scaling with respect to the number of applied threads is achieved. A discussion on the numerical performance of the proposed interface formulation is given in Section 6.3 for the simulation of large-scale interface shear tests.

### 3.6 | Modifications of constitutive continuum models for the application to interfaces

Recalling the influence of the surface roughness  $\kappa$  on the constitutive response of the interface zone (see Figure 1),  $\kappa$  has to be incorporated in the constitutive continuum models applied as interface models.  $\kappa$  is defined by Ref. 20

$$\kappa = \frac{\tan(\varphi^{\text{interface}})}{\tan(\varphi_c)} \leq 1 \quad (28)$$

with  $\varphi^{\text{interface}}$  being the friction angle of the interface and  $\varphi_c$  the critical friction angle of the soil, and can be estimated using

$$\kappa = 0.25 \log R_n + 1.05, \quad (29)$$

where  $R_n$  is the normalised surface roughness given by  $R_n = \frac{R_{\text{max}}(L = d_{50})}{d_{50}}$ .<sup>64</sup>  $d_{50}$  is the median grain size of the soil and  $R_{\text{max}}(L = d_{50})$  is the maximum surface roughness on a length  $L = d_{50}$  of the interface.

It is not desirable that the parameter sets of constitutive continuum models calibrated with the intent to be applied as continuum models have to be re-calibrated based on interface shear tests when applied as interface models. Therefore, the surface roughness is incorporated as a modification of the parameters of the constitutive continuum models without the need to perform additional interface shear tests and re-calibrate the constitutive parameters for every case. Two different constitutive continuum models are applied as interface models in this work, for which the surface roughness is incorporated as follows:

**ALGORITHM 1** Iterative calculation of the interface normal strain components

---

**Result:** Updated interface strain  $\bar{\epsilon}^{\text{interface}}$ , stress  $\bar{\sigma}^{\text{interface}}$  and state variables  $\mathbf{k}$

- 1 Divide shear strain increment  $\Delta\gamma$  in  $n_{\text{sub}}$  sub-increments  $\delta\gamma$
- 2 **for**  $i = 1, 2, \dots$  *until*  $n_{\text{sub}}$  **do**
- 3     **for**  $n = 1, 2, \dots$  *until*  $r < \text{tol}$  **do**
- 4         Calculate  $\Delta\bar{\epsilon}^{\text{interface},i}$  using  $\delta\gamma$  and  $\Delta\epsilon^{\text{interface},n}$
- 5          $\mathbf{k}^n = \mathbf{k}^i$
- 6          $\bar{\sigma}^{\text{interface},n} = \bar{\sigma}^{\text{interface},i}$
- 7         Call const. continuum model  $\bar{\sigma}^{\text{interface},n} = f(\bar{\sigma}^{\text{interface},n}, \Delta\bar{\epsilon}^{\text{interface},i}, \mathbf{k}^n)$
- 8         Calculate  $\Delta\epsilon^{\text{interface},n}$  using Eq. (22)
- 9          $r = \|\bar{\sigma}^{\text{interface},n} - \sigma'^{\text{extra}}\| / \|\sigma'^{\text{extra}}\|$
- 10     **end**
- 11     Save strain  $\bar{\epsilon}^{\text{interface},i+1} = \bar{\epsilon}^{\text{interface},i} + \Delta\bar{\epsilon}^{\text{interface},i}$
- 12     Save state variables  $\mathbf{k}^{i+1} = \mathbf{k}^n$
- 13     Save stress  $\bar{\sigma}^{\text{interface},i+1} = \bar{\sigma}^{\text{interface},n}$
- 14 **end**

---

- **Hypoplasticity with intergranular strain:** Following the work of Ref. 20, the critical friction angle  $\varphi_c$  used in the calculation of the variable  $a$  (see Ref. 29 for the complete equations) is multiplied by the roughness factor  $\kappa$ , viz.

$$a = \frac{\sqrt{3}[3 - \sin(\kappa\varphi_c)]}{2\sqrt{2}\sin(\kappa\varphi_c)}. \quad (30)$$

In addition, since the interface behaviour of rough surfaces is similar to initially dense sand while smooth surfaces tend to show a response similar to initially loose sand, the parameter  $\alpha$ , influencing the peak in the stress-strain response and the dilatancy behaviour, is modified. The pyknotropic factor  $f_d$  is calculated using

$$f_d = \left( \frac{e - e_d}{e_c - e_d} \right)^{\alpha\kappa^2} \quad (31)$$

and the barotropic factor  $f_b$  is defined by

$$f_b = \frac{h_s}{n} \left( \frac{e_{i0}}{e_{c0}} \right)^\beta \frac{1 + e_i}{e_i} \left( \frac{3p_s}{h_s} \right)^{1-n} \left[ 3 + a^2 - a\sqrt{3} \left( \frac{e_{i0} - e_{d0}}{e_{c0} - e_{d0}} \right)^{\alpha\kappa^2} \right]^{-1}. \quad (32)$$

- **Sanisand:** The critical stress ratios  $M_c$  and  $M_e$  are modified by

$$M_c = \frac{6 \sin(\kappa\varphi_c)}{3 - \sin(\kappa\varphi_c)} \quad \text{and} \quad M_e = \frac{-6 \sin(\kappa\varphi_c)}{3 + \sin(\kappa\varphi_c)}. \quad (33)$$

In analogy to the hypoplastic model, the parameter  $n_b$  (see Ref. 31 for the complete equations)

$$\alpha_\theta^b = \sqrt{\frac{2}{3}} [g(\theta, c) M e^{-n_b \kappa \psi} - m] \mathbf{n} \quad (34)$$

influencing the peak behaviour and the parameter  $A_0$

$$A_d = A_0 \kappa (1 + \langle \mathbf{z} : \mathbf{n} \rangle) \quad (35)$$

influencing the dilatancy are modified by  $\kappa$ .

#### 4 | NUMERICAL DIFFERENTIATION OF THE CONTACT CONTRIBUTIONS

The derivative (referred to as Jacobian) of the contact contributions with respect to the spatially discretised variables is required for an implicit solving scheme using the Newton-Raphson method.

A consistent Jacobian of the contact contributions is crucial for the global iteration process and to achieve fast convergence. For complex constitutive interface models the determination of the derivatives is a tedious task and prone to errors. Depending on the interface model, the correct determination of the constitutive Jacobian may even be impossible (e.g., for the hypoplastic interface model) and can only be approximated by simplifying the analytically calculated derivatives. Therefore, the Jacobian is determined using a numerical differentiation scheme. This scheme is based on the work reported in Ref. 65. The numerical differentiation secures that a consistent Jacobian is obtained in any case, hence ensuring fast convergence. It can be used in conjunction with any constitutive contact model without modifications.

The derivative of the contact contribution given by Equations (A20, A21) (see Appendix A) is first rewritten to

$$\frac{\partial \mathbf{r}_I^C}{\partial \mathbf{u}_{iI}} = \left( \mathbf{J}_I^C \right)_i, \quad (36)$$

where a mixed index notation is used to highlight the derivative with respect to component  $i$  ( $i = \{1, 2\}$  for 2D and  $i = \{1, 2, 3\}$  for 3D analyses) at node  $I$ . Assuming that the contact contribution  $\mathbf{r}_I^C$  of node  $I$  depends solely on the displacement, the Jacobian is calculated using

$$\left( \mathbf{J}_I^C \right)_i = \frac{1}{\vartheta} \left[ \mathbf{r}_I^C(\Delta \mathbf{u}_I + \vartheta \mathbf{I}_i) - \mathbf{r}_I^C(\Delta \mathbf{u}_I) \right], \quad (37)$$

where the perturbation  $\vartheta$  is introduced. Following Ref., 65  $\vartheta$  is determined by

$$\vartheta = \sqrt{EPS}, \quad (38)$$

wherein  $EPS \approx 10^{-16}$  is the machine precision. In Equation (37),  $\mathbf{I} = \text{diag}[1, 1]$  is used for 2D and  $\mathbf{I} = \text{diag}[1, 1, 1]$  for 3D analyses. Note that the derivation of contact force at one point with respect to the displacement of the connected point of the paired surface ( $\frac{\partial \mathbf{r}_I^{C,(1)}}{\partial \mathbf{u}_J^{(2)}}$  and  $\frac{\partial \mathbf{r}_J^{C,(2)}}{\partial \mathbf{u}_I^{(1)}}$ ) has to be considered. Therefore, Equation (37) has to be evaluated at least  $2 \cdot ndim + 1$  times, since the displacement of the connected point has to be perturbed as well.

For advanced constitutive interface models, the contribution of the contact forces may further be a function of contact stress  $\mathbf{t}$  and state variables  $\mathbf{k}$ , that is,  $\mathbf{r}_I^C(\Delta \mathbf{u}_I, \mathbf{t}_I, \mathbf{k}_I)$ . The state variables change with respect to the displacement, the contact stress and the state variables, described by the function  $\mathbf{f}_I(\Delta \mathbf{u}_I, \mathbf{t}_I, \mathbf{k}_I)$ . For such interface models, the numerical differentiation should incorporate the change with respect to these variables as well. The jacobian can then be calculated using

$$\left( \mathbf{J}_I^C \right)_i = \frac{1}{\vartheta} \left\{ \mathbf{r}_I^C \left[ \Delta \mathbf{u}_I + \vartheta \mathbf{I}_i, \mathbf{t}_I + \vartheta \left( \mathbf{J}_I^C \right)_i, \mathbf{k}_I + \vartheta \left( \mathbf{G}_I \right)_i \right] - \mathbf{r}_I^C \left( \Delta \mathbf{u}_I, \mathbf{t}_I, \mathbf{k}_I \right) \right\}, \quad (39)$$

where

$$\left( \mathbf{G}_I \right)_i = \frac{1}{\vartheta} \left\{ \mathbf{f}_I \left[ \Delta \mathbf{u}_I + \vartheta \mathbf{I}_i, \mathbf{t}_I + \vartheta \left( \mathbf{J}_I^C \right)_i, \mathbf{k}_I + \vartheta \left( \mathbf{G}_I \right)_i \right] - \mathbf{f}_I \left( \Delta \mathbf{u}_I, \mathbf{t}_I, \mathbf{k}_I \right) \right\}. \quad (40)$$

Equation (39) and Equation (40) have to be solved simultaneously in an iterative scheme to secure consistency.

Experience shows that using Equation (37) alone leads to fast convergence rates despite the negligence of the change of state variables with respect to displacement and stress. Equation (37) is computational advantageous compared to Equation (39), since it does not require any additional iterations and has to be evaluated only  $2 \cdot ndim + 1$  times, with  $ndim$  being the number of dimensions of the boundary value problem. Therefore, Equation (37) is used for the implementation of the numerical differentiation scheme. A comparison of the convergence rates for both approaches for the simulation of monotonic simple interface shear tests described in the next section is given in Appendix B. In addition, the superior

convergence rates obtained using the numerical differentiation schemes over a scheme approximating the derivatives of the hypoplastic interface model is demonstrated in Appendix B.

For contact analyses without friction or a simple Coulomb friction model the analytically derived constitutive Jacobian is preferred since the contact algorithms have to be run only once.

## 5 | SIMULATION OF SIMPLE INTERFACE SHEAR TESTS

To show the performance of the proposed constitutive interface models, simple interface shear tests are simulated. A schematic sketch of the tests, the difference between simple and direct shear tests as well as the definition of the normal stress and strain components for the test conditions are given in Figure 5. The considered tests have been performed by Fakharian<sup>50</sup> and Fakharian & Evgin.<sup>45</sup> The experimental campaign comprises tests with constant normal stress and tests with constant normal stiffness. The soil sample had dimensions of  $100 \times 100 \times 20$  mm.

Monotonic as well as cyclic tests with up to 50 cycles have been performed. Different soils have been studied but only tests using a crushed silica sand are considered for the numerical analyses. Since neither the material is available nor any triaxial test data exists, the material constants required for the constitutive interface models are estimated based on parameters for a similar material. A crushed quartz sand (termed "L4C"), which has a grain size distribution very similar to the silica sand used in the interface tests and the same  $d_{50} = 0.6$  mm, is used. The parameters of Hypoplasticity with intergranular strain, determined based on laboratory tests (index, oedometer and triaxial tests), are provided in Table 1. Note that no "tuning" of the parameters is performed since the comparison of the different interface formulations is focused here and not the comparison with the experimental data. Note in addition that the investigations in this section are restricted to the hypoplastic interface model. The Sanisand interface model is later applied in Section 6 for the simulation of large-scale interface shear tests.

### 5.1 | Tests with monotonic loading

Only tests with comparatively modest values of normal contact stress are considered, excluding those with higher stress. Particle breakage occurred in the tests with higher stress, which can not be considered with the interface models developed in this work. Simple interface shear tests with constant normal stress of 100 kPa, an initial relative density of  $D_{r0} = 0.88$  and sand-blasted steel surface are considered. The surface is assumed to be nearly perfectly rough ( $\chi = 0.9$ ) in the numerical analysis. An interface thickness of  $5 \cdot d_{50} = 3$  mm is assumed. The intergranular strain tensor is assumed to be initially fully mobilised in the direction of shearing, such that no increased shear stiffness due to the intergranular strain extension exists initially. During the test, the intergranular strain tensor evolves due to strain in the normal interface direction. The initial stress in the continuum is calculated assuming a lateral stress coefficient of  $K_0 = 0.5$ .

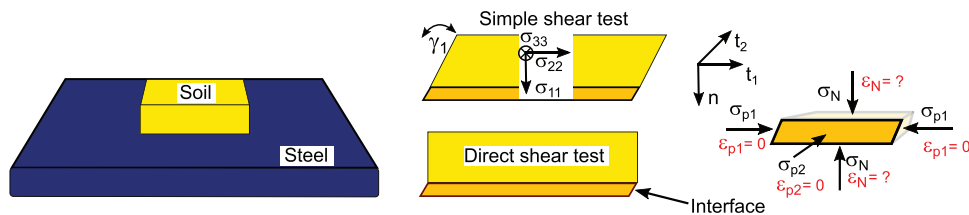
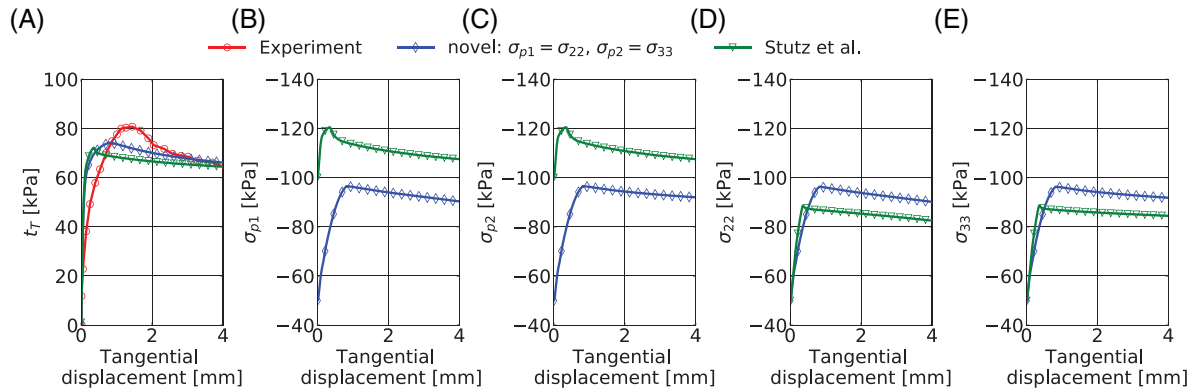


FIGURE 5 Schematic sketch of the interface shear tests, the different test conditions for simple and direct shear tests, the definition of the normal continuum stresses and the definition of the normal stress and strain components in the interface for the test conditions

TABLE 1 Parameters of the hypoplastic model with intergranular strain extension for the crushed quartz sand "L4C"

$\varphi_c$	$e_{i0}$	$e_{c0}$	$e_{d0}$	$h_s$	$n$	$\alpha$	$\beta$	$m_R$	$m_T$	$R$	$\beta_R$	$\chi$
$36^\circ$	1.320	1.149	0.763	4.5 GPa	0.28	0.094	1.2	2.4	1.2	$10^{-4}$	0.3	1.5



**FIGURE 6** Results of the simulation of a simple interface shear test using either the novel approach for the calculation of the stress conditions in the interface element or the approach by Stutz et al. The interface shear stress and the interface normal stress components  $\sigma_{p1}$  and  $\sigma_{p2}$  versus the tangential displacement  $u_T$  of the steel plate are displayed in plot a), b) and c), respectively. For the novel approach, the interface normal stress components  $\sigma_{p1}$  and  $\sigma_{p2}$  are obtained from the continuum ( $\sigma_{p1} = \sigma_{22}$  and  $\sigma_{p2} = \sigma_{33}$ ). In addition, the continuum normal stress components  $\sigma_{22}$  and  $\sigma_{33}$  versus the tangential displacement are given in plots d) and e), respectively

Idealising the interface shear box as single element test (one linear finite element with one integration point<sup>4</sup>), the normal stress component  $\sigma_{p1}$  is non-constant and the corresponding strain is zero ( $\varepsilon_{p1} = 0$ ) (see Figure 5). The normal stress component  $\sigma_{p2}$  is also non-constant and for the strain  $\varepsilon_{p2} = 0$  holds.

Note that due to the aforementioned boundary conditions of the shear test, only  $\varepsilon_N$  is non-zero using Equation (22). The other normal strain components are zero since the normal stress components  $\sigma_{p1}$  and  $\sigma_{p2}$  develop identical to the corresponding continuum stresses. This does not need to be set manually for the novel interface formulation but results automatically from the stress and strain conditions. Note that this is due to the boundary conditions of the simple interface shear test and not the case for more complex BVPs in general. For the numerical model, the vertical displacement of the top nodes is enforced to be identical by using a multi-point constraint. This constraint accounts for the rigid top plate used to apply the normal stress in the experiment. Note that for the implementation of the original approach by Stutz et al. in numgeo, which is applied for comparison purposes in the following, the same sub-increment scheme and error control as described in Section 3.5 are used. Identical values for tolerated error and sub-increment size are used for both approaches. In addition, the identical implementation of the hypoplastic continuum model is utilised.

The results of the experiment and those of the simulations using the novel approach for the stress conditions in the interface element ( $\sigma_{p1} = \sigma_{22}$  and  $\sigma_{p2} = \sigma_{33}$ ) and the approach by Stutz et al. are displayed in Figure 6. The shear stress  $t_T$  and the normal stress components  $\sigma_{p1}$  and  $\sigma_{p2}$  of the interface are plotted versus the tangential displacement of the steel plate. In case of the simulation with the novel approach both interface normal stress components are obtained from the continuum using the procedures described in Section 3.3. The normal continuum stress components  $\sigma_{22}$  and  $\sigma_{33}$  versus the tangential displacement are given in Figure 6D,E as well.

The shear stress versus tangential displacement plot demonstrates that both interface formulations predict different peak and residual values of shear stress. The simulation using the approach by Stutz et al. results in a lower peak and residual shear stress compared to the novel approach. Since the initial stiffness is higher due to the higher initial mean stress in the interface, the approach by Stutz et al. furthermore results in an earlier peak in shear stress with respect to the tangential displacement. Compared to the experiment the peak is also underestimated using the novel interface formulation, which could be enhanced using a larger value of surface roughness  $\kappa$  or a larger value for the parameter  $\alpha$  of the hypoplastic model. In case of the novel interface formulation using  $\sigma_{p1} = \sigma_{22}$  and  $\sigma_{p2} = \sigma_{33}$ , the normal interface and normal continuum stress components match, as is visible from the comparisons of Figure 6B with Figure 6D and Figure 6C with Figure 6E. The approach by Stutz et al. results in a strong jump of normal stress components between interface and continuum.

Despite the higher values of interface normal stress components (compared to the novel approach assuming  $\sigma_{p1} = \sigma_{22}$  and  $\sigma_{p2} = \sigma_{33}$ ), a slightly lower residual shear resistance is observed in case of the simulation using the approach by Stutz et al. This is due to the lower continuum normal stress components as is visible from Figure 6D and Figure 6E. Therefore, the continuum is the "weak link" (the interface and the continuum respond as in *series*, and not as in *parallel*) using the approach by Stutz et al.

The comparison of the different interface formulations shows that the choice of the boundary conditions of the interface element influences the mechanical response. However, both formulations give reasonable results in terms of shear stress versus tangential displacement compared to the results of the experiment. It is not surprising that only small differences in terms of shear stress exist, since the normal strain in the interface is almost identical to the normal strain of the adjacent continuum element (however, the approach by Stutz et al. gives less normal strain in the interface compared to the continuum due to the higher mean stress in the interface). Since the shear stress in the interface and the continuum is also identical, but all other strain components are zero, the assumptions of the approach by Stutz et al. hold. However, as is demonstrated for the large-scale cyclic interface shear tests in Section 6, the different approaches for the interface zone can have a distinct influence on the predicted shear stress, when the stress and strain conditions are more complex.

In order to judge the performance of the different interface models for perfectly rough conditions in comparison to a simulation without interface element, corresponding simulations are presented in Appendix C. In addition, a simulation with an initialisation of the normal interface stresses using the initial continuum stresses for the approach by Stutz et al. is given there. Despite the differences in the definition of the normal stress components in the interface element, all approaches for the interface element give shear stresses very close to the simulation without an explicitly modelled interface zone. However, when initialising all interface normal contact stresses identical to the normal contact stress, higher shear stresses are observed for the approach by Stutz et al.

## 5.2 | Tests with cyclic loading

The cyclic interface shear tests have been performed by Fakharian<sup>50</sup> and Fakharian & Evgin<sup>45</sup> as well. In contrast to the monotonic tests, constant normal stiffness conditions are considered. The initial normal stress is 300 kPa.

The simulation of a test with a normal stiffness of  $K = 400$  kPa/mm and a tangential displacement amplitude  $u_T^{\text{ampl}} = 0.75$  mm using the hypoplastic interface model is displayed in Figure 7 for the novel formulation and the formulation by Stutz et al. Figure 7A and Figure 7C display the shear stress versus tangential displacement for the first ( $N = 1$ ) and 11th ( $N = 11$ ) cycle, comparing the results of the experiment and the simulations using the two approaches. The initial loading and un-loading is well reproduced by both simulations. The residual shear stress at the end of the first complete cycle is; however, too large compared to the measured value. Both the results of the simulations and the results of the experiment show much lower values of shear stress for the 11th cycle compared to the first cycle. In case of the simulations, the reduction of the shear stress is much more pronounced than for the experiment. This could be remedied by choosing another set of parameters for the intergranular strain (e.g., increasing the stiffness multipliers at strain reversal). However, since the present work aims for the comparison of the different interface formulations, an optimisation of parameters is not performed here. The normal displacement versus tangential displacement plots given in Figure 7B and Figure 7D show that the compaction (negative values of  $u_N$  indicate reduction in soil volume) of the soil caused by the first cycle is well reproduced by both interface formulations. The compaction during the first quarter of the cycle is very well predicted, while the dilatancy during the third quarter is not well captured by the simulation. In addition, the compaction during the last quarter of the first cycle is underestimated. The compaction at the 11th cycle is overestimated, however. Larger normal displacement is predicted by the simulations in comparison to the experiment. During the 11th cycle almost no dilatancy and no accumulation of compaction occurs in the simulations, which stands in contrast to the curve of the

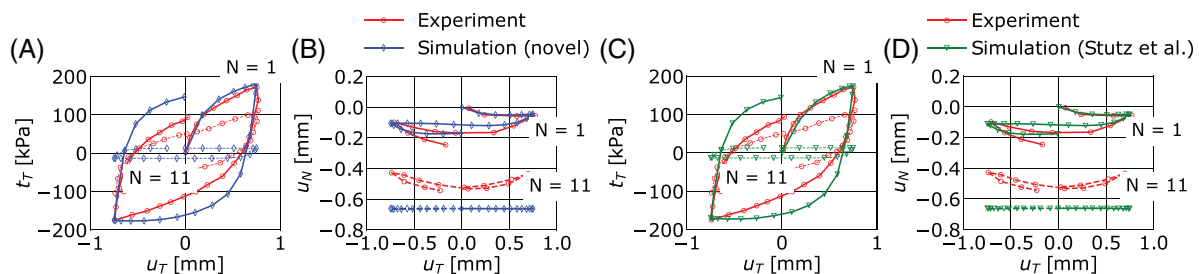


**FIGURE 7** Results of the simulations of a cyclic simple interface shear test with constant normal stiffness using either the novel hypoplastic interface formulation (plots a and b) or the approach by Stutz et al. (plots c and d) in comparison to the measurements made in the experiment. Plot a), c) and b), d) display the shear stress  $t_T$  and normal displacement  $u_N$  versus tangential displacement  $u_T$  at  $N = 1$  and  $N = 11$  cycles, respectively

experiment. Overall, the differences between the predictions by the two interface formulations are very small (see the previous section for an explanation why the results are similar). To inspect if this holds true for a more complex BVP, large-scale cyclic interface shear tests are studied in the next section.

## 6 | LARGE-SCALE INTERFACE SHEAR TESTS

The large-scale interface shear test set-up was originally developed by Rebstock<sup>66</sup> at the Institute of Soil Mechanics and Rock Mechanics at KIT, Karlsruhe. It has later been improved by Vogelsang<sup>43,67</sup> and has been used to study the interface behaviour of soil for complex geometrical conditions and varying values of surface roughness.

### 6.1 | Experimental set-up and numerical model

The dimensions of the test set-up are schematically shown in Figure 8A. Dry sand has been pluviated in layers into the steel-framed box. The box is 1.2 m wide, 0.5 m deep, and 2 m high. The wall on the right-hand side is made of four segments that can be shifted up- or downwards with a hydraulic drive. The resulting forces were measured with load cells attached to the segments in vertical and horizontal direction. Each segment has a width of 0.5 m and a height of 0.6 m. The second segment from below is sanded, thus its surface can be assumed as perfectly rough with  $\kappa \approx 1$ . The other three segments are made of stainless steel and have a smooth surface with a roughness of  $\kappa \approx 0.35$ .<sup>43</sup> The imposed movement of the wall for the test considered for the numerical analysis is supplied in Figure 8A. A cyclic displacement-time history with a 3 mm downwards phase followed by 1 mm upwards movement was used. The monotonic tests performed by Vogelsang are not considered here since the initial phase of the cyclic test is equivalent to the monotonic path and the results are therefore to some extent redundant. The considered test had an initial height of the sand volume of 1.56 m and a relative density of  $D_{r0} = 70\%$ . The segment at the bottom of the box overlapped the lower boundary of the sand volume by 9 cm at the start of the test.

Throughout the experiments performed by Vogelsang the so-called "Karlsruhe Sand", which is a medium coarse sand, has been used. The index parameters are supplied in Table 2. During the last decades, different sands have been referred

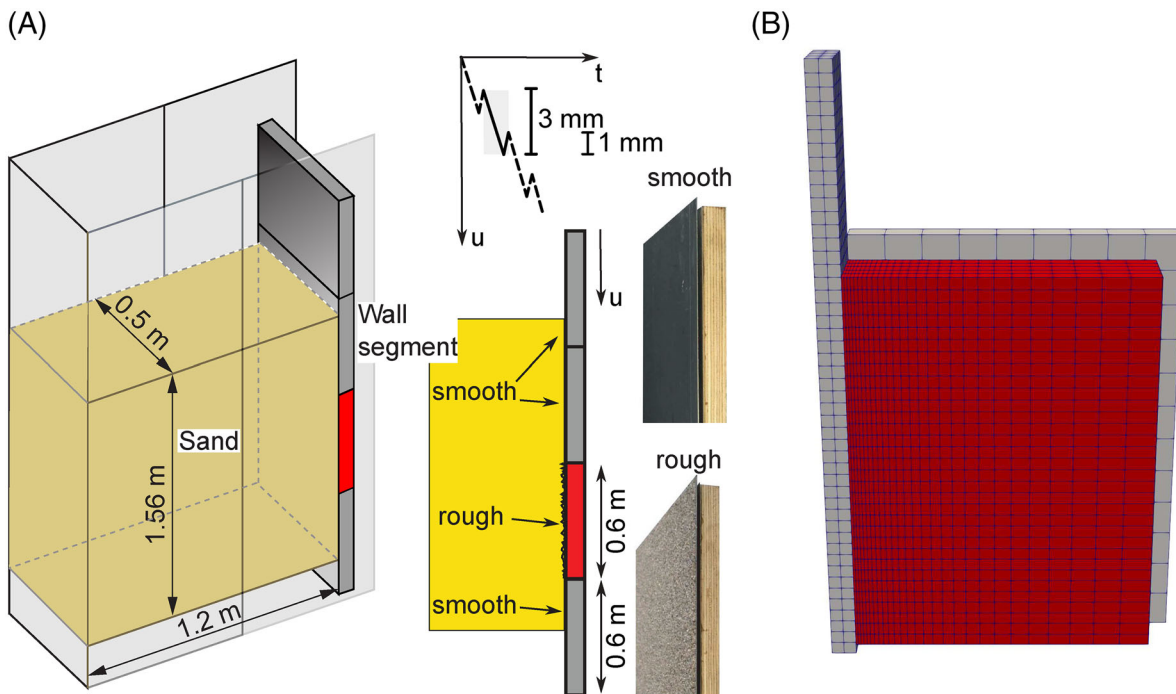


FIGURE 8 (A) Large-scale interface test set-up (modified from Ref. 43) with dimensions, photos of the surfaces of the different wall segments and imposed displacement-time history of the wall. (B) Finite-element model adopted for the numerical analysis of the test

TABLE 2 Index parameters of "Karlsruhe Sand"

Parameter		Quantity	Unit
Grain density	$\bar{\rho}_s$	2.65	[g/cm <sup>3</sup> ]
Median grain size	$d_{50}$	0.55	[mm]
Coefficient of uniformity	$C_U$	1.5	[-]
Maximum void ratio	$e_{\max}$	0.857	[-]
Minimum void ratio	$e_{\min}$	0.555	[-]
Critical friction angle	$\varphi_c$	33.1	[°]

TABLE 3 Parameters of the hypoplastic model with intergranular strain extension for "Karlsruhe Sand"

$\varphi_c$	$e_{i0}$	$e_{c0}$	$e_{d0}$	$h_s$	$n$	$\alpha$	$\beta$	$m_R$	$m_T$	$R$	$\beta_R$	$\chi$
33.1°	0.979	0.851	0.549	19 GPa	0.285	0.1	0.32	2.4	1.2	$5 \cdot 10^{-5}$	0.08	7

TABLE 4 Parameters of the Sanisand model for "Karlsruhe Sand"

$p_a$	$e_0$	$\lambda_c$	$\xi$	$M_c$	$c$	$m$	$G_0$
100 kPa	1.1	0.25	0.35	1.3	0.88	0.05	70
$\nu$	$h_0$	$c_h$	$n_b$	$A_0$	$n_d$	$z_{\max}$	$c_z$
0.05	8	0.35	1.3	0.8	0.8	60	2000

to as "Karlsruhe Sand", which can differ significantly in their grain sizes and shapes. An extensive experimental study and description of the "Karlsruhe Sand" used in the experiments considered here is given in Ref. 67.

A 3D model with linearly interpolated and reduced integrated elements is used, which is displayed in Figure 8B. The side wall is considered in the model in order to take into account the friction at the soil-structure interface. The symmetry of the test is utilised such that only a soil volume of  $0.25 \times 1.2 \times 1.56 \text{ m}^3$  is modelled. Vertical and horizontal displacement constraints are introduced at the bottom of the soil. The reason for constraining the horizontal displacement is the comparably rough surface of the bottom surface of the container. In accordance with the preliminary numerical analysis performed by Vogelsang using a simple Coulomb friction model,<sup>43</sup> the pluviation of the soil is taken into account by incrementally increasing the gravity acting on the soil mass. The initial value of gravity  $g = 2 \text{ m/s}^2$  is increased by increments of  $2 \text{ m/s}^2$  until  $g = 10 \text{ m/s}^2$  is reached. Discussion on the importance of incrementally increasing the gravity in order to correctly model the initial stress state can be found in Ref. 25, 43, 68. The modelling of the pluviation process leads to lower final vertical and horizontal stresses because of the shear stresses developing at the sides of the container (arching effect). A geometrically non-linear calculation (updated Lagrangian) is performed. The Zaremba-Jaumann stress rate is used in order to ensure an objective stress rate. For the constitutive modelling of the interface either the hypoplastic model with intergranular strain extension, the Sanisand model or the Coulomb friction is used. The hypoplastic model is used for the continuum independently of the applied interface model. The novel formulation of the interface element according to Section 3.3 is used. Both normal stress components ( $\sigma_{p1}$  and  $\sigma_{p2}$ ) are extrapolated from the continuum to the interface element. In addition, a simulation with the approach by Stutz et al. is performed.

The constitutive parameters of the hypoplastic and the Sanisand model have been calibrated based on numerous oedometric compression, monotonic and cyclic triaxial tests on "Karlsruhe Sand" reported in Ref. 37. Tests with low effective stress level have been used in order to best represent the conditions in the model tests. The parameters of the hypoplastic model are given in Table 3 and those for Sanisand in Table 4. If not stated otherwise, the shear band thickness is assumed to be  $d_s = 6 \text{ mm}$ , which is  $\approx 11 \cdot d_{50}$ , for all segments. The initial lateral earth pressure coefficient for both directions prior to the incremental increase of gravity is assumed to be  $K_0 = 0.5$ . Friction at the smooth segments as well as the side wall is considered using the Coulomb friction model with a friction coefficient of  $\mu = \tan(\delta) = 0.25$  ( $\kappa \approx 0.35$ ) and a tangential stiffness of 6000 kN/m. In accordance with the observation that smooth surfaces can be adequately modelled using the Coulomb friction model (see Section 3), preliminary analyses using the sophisticated interface models also for the smooth segments and the side walls gave similar results as simulations using the Coulomb model. In addition, only 20 % of the total shear force of the moving wall originates from the smooth segments while 80 % is mobilized at the rough segment.<sup>43</sup> Therefore, due to the improved computational performance, the Coulomb model is applied for the smooth surfaces.

To the author's best knowledge only very few of the advanced constitutive interface models proposed in the literature have been applied to complex BVPs with cyclic shearing such as the large-scale interface tests considered here. Examples for the application of advanced constitutive interface models to more complex BVPs can be found in Ref. 14, 19. The rare application to complex BVPs is believed to be due to the inferior convergence rate faced when introducing strongly non-linear interface models in implicit calculations. These problems are to some extent circumvented in the numerical implementations used in the present work, since a consistent Jacobian is secured by the numerical differentiation scheme introduced in Section 4. It is worth noting that simulations of the large-scale interface tests using an analytically derived Jacobian of the contact contributions did not converge.

## 6.2 | Results of the simulations

The results of the experiments and the simulations are evaluated in terms of average shear and normal stress measured at the rough segment. During the test, the forces acting normal and tangential to this segment were measured. Based on these forces, the average stress of the segment was calculated. The results of the tests and those of the simulations using the hypoplastic model for the interface as well as for the continuum are given in Figure 9. Predictions by both the novel interface approach and the approach by Stutz et al. are given. Two cyclic movement phases are studied. A positive value of wall displacement indicates downwards directed movement. Both simulations capture the slightly negative shear stress prior to the wall movement caused by the soil assembling process well. Likewise, the initial normal stress is in good accordance with the measurements of the experiment. Both the shear and normal stress increase when the wall starts to move downwards, which is well predicted by both simulations qualitatively and quantitatively. The values reached at a wall movement of 3 mm are in good agreement with the measurements of the test. The approach by Stutz et al. results in an earlier and lower peak of the shear stress reached before 3 mm wall displacement. When the wall movement is reversed, both the shear and the normal stress reduce. In case of the normal stress, both simulations capture the rapid reduction at the initial stage of the reversed movement but show much higher values compared to the measurements for larger wall displacement. Since the simulation using the approach by Stutz et al. starts with a lower value of normal stress at the point of reversal, the minimum value reached at a wall displacement of 2 mm is also lower, fitting better to the experiment compared to the novel approach. Due to this overestimation of the normal stress by both simulations, the reduction in shear stress after reversal is in turn overestimated, since the yielding shear stress is in magnitude much higher compared to the experiment. The minimum shear stress reached during the upwards movement in the experiment is much higher due to the lower normal stress.

Similar observations are made for the second cycle. In terms of normal stress the discrepancies between the measurements and the results of the simulations increase for both the downwards and the upwards movement phase. For both wall movement phases the increase respectively decrease in normal stress is too small in the simulations compared to the measurements. Compared to the novel approach, the approach by Stutz et al. shows much lower values of shear and normal stress during the second cycle, resulting in a worse accordance with the measured values. In addition, the

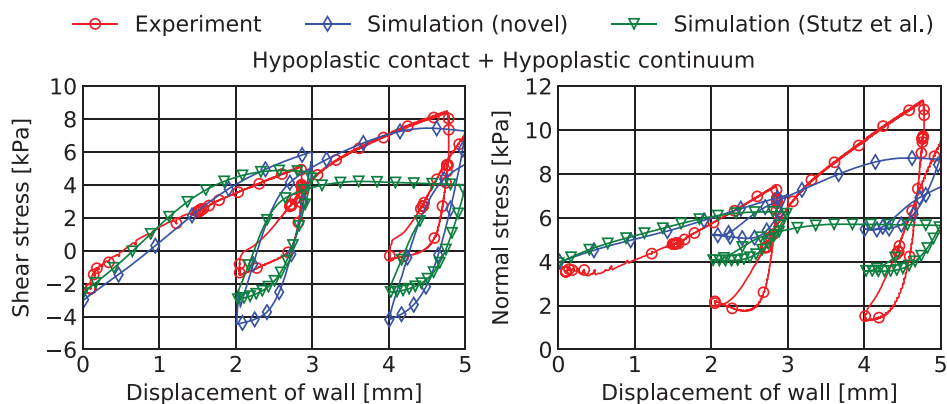
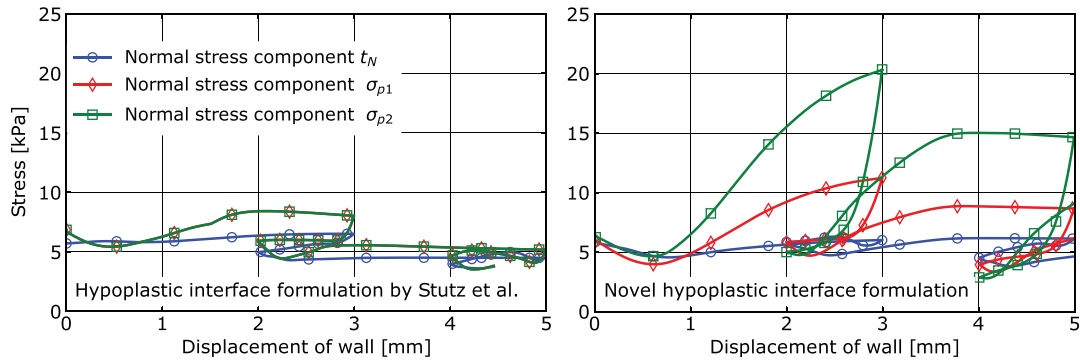


FIGURE 9 Average shear stress and normal stress of the rough segment versus displacement of the wall for the values measured in the experiment and the simulations using the proposed hypoplastic interface model (novel) and the approach by Stutz et al., respectively



**FIGURE 10** Development of the normal stress components in an interface point at the lower half of the rough segment for the approach by Stutz et al. and the novel approach using the hypoplastic interface formulation

continuous increase in both stress components during the downwards movement in the second cycle is not reflected. Overall, the novel approach leads to higher maximum shear stress, in particular for the second cycle. This is reasonable, since the vertical stress of the continuum is taken into account by the novel approach. Since the vertical stress is larger than the horizontal stress components, higher mean stresses act in the interface resulting in a higher shear resistance. This is also visible from Figure 10, which depicts the development of the normal stress components in an interface point at the lower half of the rough segment for the two approaches. The component  $\sigma_{p1}$  corresponds to the horizontal stress component, while  $\sigma_{p2}$  is acting in vertical direction (in this particular case the orientations of the normal stress components in the interface are identical to the global coordinate axes). Much larger values of  $\sigma_{p1}$  and  $\sigma_{p2}$  develop during the wall movement using the novel approach. Especially the vertical stress ( $\sigma_{p2}$ ) increases significantly, which can be explained by an impaction of soil (i.e., a zone of stress concentration) between the rough segment and the bottom of the container during the downwards movement. This is visible from the spatial distribution of vertical stresses given in Figure 13, which is discussed in more detail later. Such influences resulting from the geometry and boundary conditions of the BVP are only indirectly considered by the approach of Stutz et al. The horizontal stress component ( $\sigma_{p1}$ ) obtained with the novel approach, however, does not differ significantly from the values obtained using the approach by Stutz et al. When the wall moves upwards, values lower than the initial state are observed. Slightly lower values are obtained for the approach by Stutz et al. at maximum upwards movement, which explains the slightly lower absolute values of shear stress observed in Figure 9. Figure 10 demonstrates that the normal stress components in the interface zone diverge considerably during shearing and the assumption of  $\sigma_{p1} = \sigma_{p2}$  is not valid for this BVP.

The corresponding simulation using the Coulomb friction model for the rough segment is presented in Figure 11. The normal and tangential stresses prior to the movement of the wall are again in good accordance with the measured values. Both the shear and normal stress increase less in the initial wall displacement phase compared to the simulation using the hypoplastic interface models. The maximum shear and normal stresses measured at a wall displacement of 3 mm in the

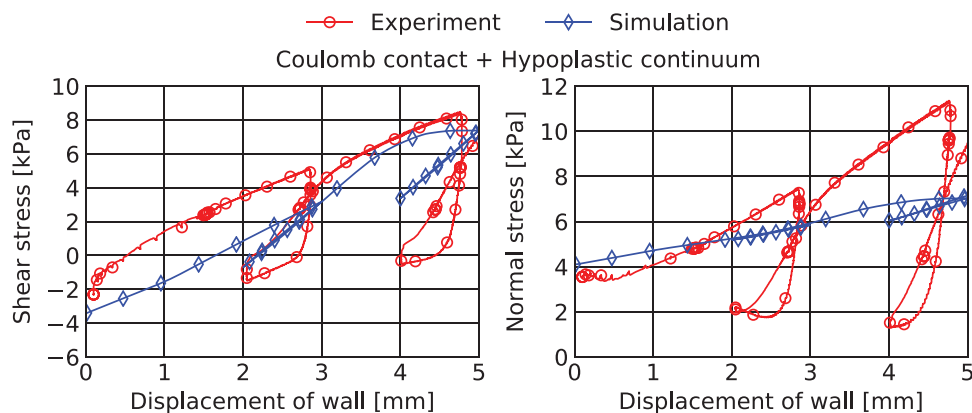


**FIGURE 11** Comparison of the experimental results with a simulation using a Coulomb interface model

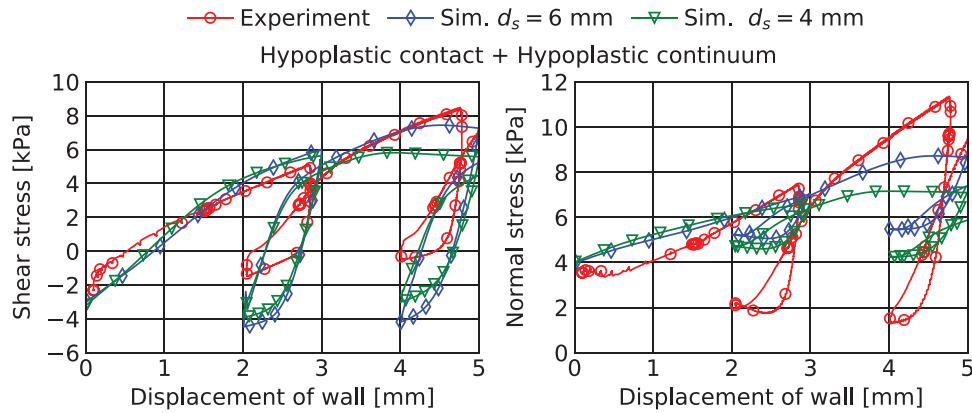


**FIGURE 12** Average shear stress and normal stress of the rough segment versus displacement of the wall for the values measured in the experiment and the simulation using the proposed hypoplastic interface model comparing two different values of shear band thickness  $d_s$

experiment are both underestimated by the simulation. No sliding of the soil at the rough segment is encountered, which is visible by the steady increase in shear stress without approaching a constant maximum value. When the wall moves upwards again, both the shear and the normal stress reduce with almost the same inclination in the stress-displacement diagram as during the downwards movement. This is in contrast to the measured stress-displacement histories, which show a much stronger reduction in stress during the first  $\approx 0.2$  mm of upwards movement. The reduction in the normal stress during this phase is strongly underestimated by the simulation using the Coulomb interface model. The simulations using the hypoplastic models show a much better accordance with the experimental results, capturing the strong initial reduction in normal stress.

The results demonstrate the large influence of the constitutive interface model on the simulation results. Despite using the hypoplastic model for the continuum, the simulation using the Coulomb friction model is not capable to capture many aspects of the interface behaviour. The proposed hypoplastic interface model is able to predict the changes in the inclinations of the stress-displacement curves at reversals of the wall displacement direction as well as the significant increase in normal stress with downwards wall movement.

The shear band thickness is a parameter of the interface model which adds a considerable uncertainty due to its wide range of possible values (see Section 3.4). Therefore, a comparison for values of the shear band thickness of  $d_s = 6$  mm and  $d_s = 4$  mm  $\approx 7 \cdot d_{50}$  is provided in Figure 12. The hypoplastic model is used for the interface as well as for the continuum. Only the novel interface formulation is used. For the first phase of the wall movement both simulations show a comparable change in shear and normal stress. A slightly faster mobilisation of stress is observed for  $d_s = 4$  mm due to the higher shear strain in the interface element for the same wall movement. Furthermore, a slightly stronger reduction in normal stress during the first upwards phase is observed for  $d_s = 4$  mm, which is in better accordance with the experimental values compared to the simulation using  $d_s = 6$  mm. In the subsequent downwards movement of the wall, the simulation using  $d_s = 4$  mm results in a higher maximum shear stress compared to the simulation with  $d_s = 6$  mm. The simulation with  $d_s = 6$  mm shows larger amplitudes of shear stress compared to the simulation with  $d_s = 4$  mm. This difference seems to increase with ongoing cyclic wall movement since the differences in the shear stress amplitude are larger for the second cycle compared to the first one. It can be noted that the influence of the shear band thickness is low for the first cycle but seems to increase with ongoing cyclic loading.

The spatial distributions of the (continuum) shear stress component  $\sigma_{31}$ , of the horizontal stress  $\sigma_{11}$  and of the vertical stress  $\sigma_{33}$  are provided in Figure 13 at the time of the maximum downwards movement of the wall in the first cycle. The hypoplastic model is applied for the contact and the continuum. Only the novel interface formulation is used. The rough segment is easily identifiable by the large shear stress acting in the soil adjacent to it. Merely small values are observed for the soil adjacent to the smooth segments. At the same wall movement, the horizontal and vertical stresses are also significantly increased in the vicinity of the rough segment. The horizontal stress acting close to the smooth segment below the rough segment is noticeably reduced due to the wall displacement. From the field of vertical stress, a zone in the shape of a triangle with high values of stress is visible (impacted soil zone). This has already been mentioned previously and is, since the vertical stress enters the interface formulation, one of the reasons why the novel interface formulation predicts higher shear stresses at the rough segment during the downwards movement of the wall compared to the approach by Stutz et al.

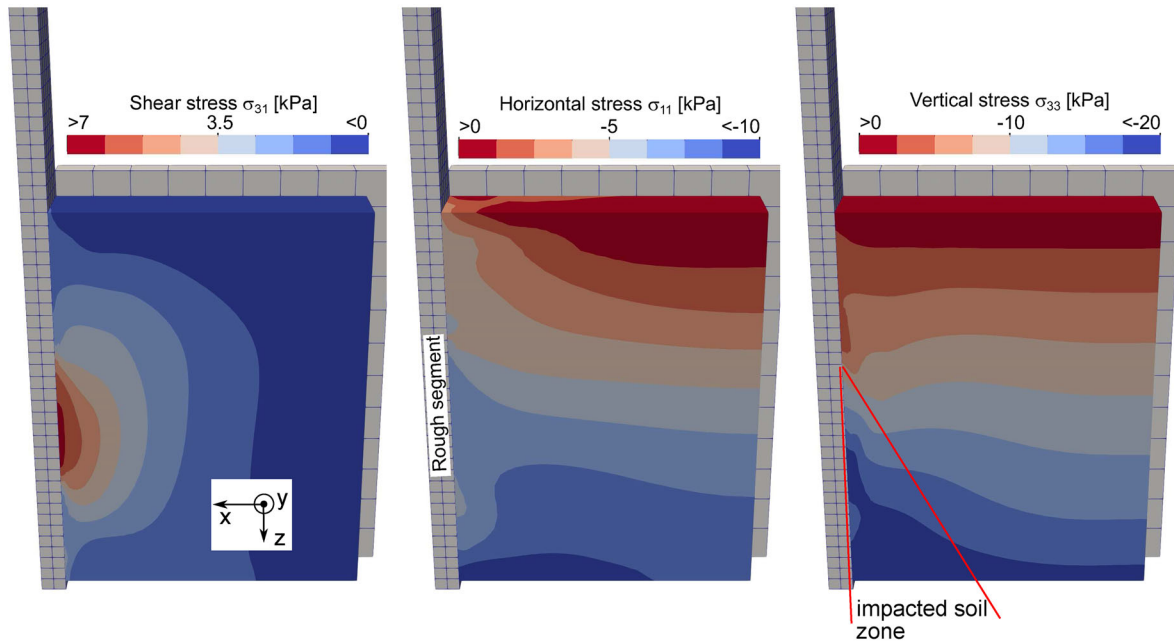


FIGURE 13 Spatial distribution of shear stress  $\sigma_{31}$ , horizontal stress  $\sigma_{11}$  and vertical stress  $\sigma_{33}$  at the time of maximum downwards movement of the wall in the first cycle using the hypoplastic model for both the interface and the continuum

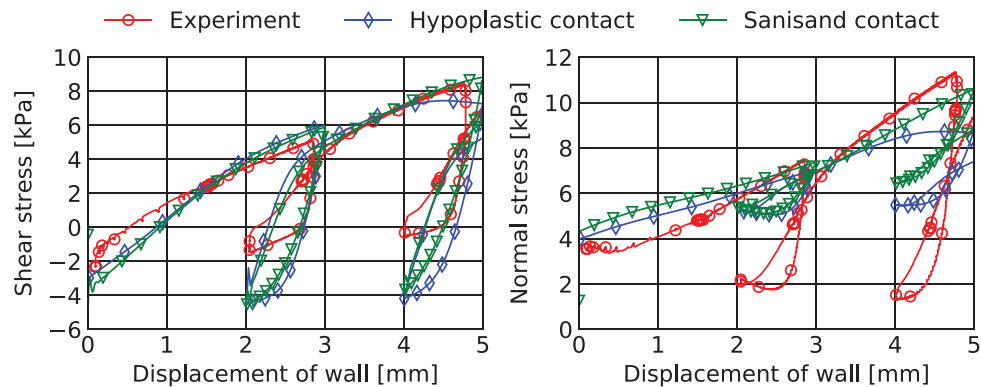


FIGURE 14 Comparison of the experimental results with a simulation using the hypoplastic and the Sanisand interface model in the framework of the novel interface formulation

In another comparison, the Sanisand interface model proposed in Section 3.6 is applied. Note that the hypoplastic model is used for the continuum nevertheless. Simulations using Sanisand for both the interface and the continuum give similar results but the convergence using the Sanisand model for the continuum is worse compared to the application of the hypoplastic continuum model. Using the Sanisand interface model both the shear and the normal stress at the downwards movement phases of the wall are better captured than using the hypoplastic interface model as is visible from Figure 14. During the upwards movement, however, the normal stress is overestimated in comparison to the values measured in the experiment as well.

The comparisons of the simulations with the results of the model tests show that the constitutive interface model is of great importance for the mechanical response of rough soil-structure interfaces. In particular, the stress development in the interface due to the cyclic movement of the wall cannot be adequately captured using a Coulomb friction model. The novel interface models proposed herein are found to deliver a better reproduction of the measurements than the approach by Stutz et al., highlighting the importance of the stress conditions in the interface element. However, independent of the employed interface formulation, the reduction of the normal stress at the rough segment at wall movement reversal is not well predicted by the numerical simulations. Since considerable shear strains are developing in the continuum during the

**TABLE 5** Number of (global) iterations, total (physical) time, and (physical) time spent in the contact routines for the different interface models and formulations

Simulation	No. of iterations	Total time [s]	Time contact [s]
Coulomb friction	2600	5969	618
Novel hypoplastic interface	2950	8540	2524
Novel Sanisand interface	2710	9343	3459
Hypoplastic interface by Stutz et al.	2730	8504	2463

The contact routines, element loop and the solver are all run with four native cores (one Intel Core i9 9900K processor with four cores run with the base-frequency of 3.6 GHz without utilising Hyper-threading is used)

wall movement, it would be interesting to study if a micro-polar continuum formulation of the hypoplastic model (see e.g., Ref. 69, 70) gives different results than the standard formulation employed herein.

### 6.3 | Computational performance

Table 5 gives the total number of iterations, the total time to finish the calculation and the total time spent in the contact routines for the simulations of the large-scale interface shear test using the different interface models and formulations. Unsurprisingly, the Coulomb friction requires the fewest number of iterations and results in the shortest calculation time. The time spent in the contact routines is only 10 % of the total time of the simulation. For the novel hypoplastic interface formulation more iterations and much more time is required. The ratio of time spent in the contact routines to total time increases to 30 %. An even worse computational performance is observed using the novel interface formulation in combination with the Sanisand model, even though slightly less iterations are required. Approximately 40 % more time is spent in the contact routines compared to the hypoplastic interface model. These differences are not due to the formulation as interface models but result from the general formulation and implementation of the (continuum) constitutive models underlying the interface formulation. The implementation of the hypoplastic continuum model employs an adaptive sub-increment scheme with error control whereas for the Sanisand model an explicit sub-stepping scheme is employed (see Ref. 37, 40 for details on the implementation of the constitutive continuum models).

Compared to the novel hypoplastic interface formulation the approach by Stutz et al. shows a slightly better numerical performance. This is because no extrapolation of stresses from the continuum is required. In addition, fewer global iterations are required, which can be explained by the lower values of shear stress developing at the rough segment, leading to less changes in strains and stresses in the continuum and the interface.

## 7 | SUMMARY AND CONCLUSIONS

A novel formulation for the application of advanced constitutive continuum models as interface models has been proposed in this work. Constitutive continuum models such as Hypoplasticity with intergranular strain extension and the Sanisand model can be applied as interface models using the presented approaches with only minor modifications of the constitutive equations. In order to obtain the stress state in the interface, an extrapolation of the stress from the adjacent continuum to the interface has been proposed, which avoids the violation of the equilibrium conditions being the case using existing approaches. The consequences of the different definitions of the stress conditions in the interface have been demonstrated by the simulation of simple interface shear tests with monotonic or cyclic loading. Subsequently, the simulation of large-scale cyclic interface shear tests using the proposed interface models has been presented. Compared to simulations using a simple Coulomb friction model, simulations using the hypoplastic interface model were in better agreement with the measurements of the experiment. Using the approach by Stutz et al. lead to an underestimation of shear stresses and a slightly worse accordance with the experimental data compared to the novel interface formulation because the increased vertical stresses cannot directly be taken into account in the interface. Using the novel Sanisand interface model, an even better accordance with the measurements compared to the novel hypoplastic interface model was achieved. The advanced interface models were found to be able to capture the different interface behaviour at un- and reloading, which is not possible using the Coulomb friction model.

The proposed interface formulation can be viewed as a more general approach as the one presented by Stutz et al., allowing to flexibly account for the boundary conditions and (initial) stress conditions of the interface zone. As has been demonstrated by the back-analysis of the large-scale interface shear test, taking into account the differences in the normal stress components in the interface zone can influence the outcome of the results considerably.

## ACKNOWLEDGMENTS

The authors are grateful to Jakob Vogelsang for providing the experimental data.

Open access funding enabled and organized by Projekt DEAL.

## DATA AVAILABILITY STATEMENT

Data available on request from the authors

## ORCID

Patrick Staubach  <https://orcid.org/0000-0002-1788-4880>

Jan Machaček  <https://orcid.org/0000-0003-4849-5754>

Torsten Wichtmann  <https://orcid.org/0000-0002-9250-7014>

## ENDNOTES

- <sup>1</sup> This is not the case for the (first) approach presented in Ref., <sup>22,27</sup> where a projection of the continuum model to the interface zone is used. This requires the assumption of Lode's angle to be zero and has thus far only been used together with rather simple elasto-plastic constitutive continuum models.
- <sup>2</sup> numgeo (Machaček & Staubach, see Ref. 35–42,75 and <http://www.numgeo.de>) is a stand-alone finite element program developed by the first two authors for the solution of non-linear, coupled (dynamic) geotechnical BVPs.
- <sup>3</sup> The stress tensor of the interface  $\sigma^{\text{interface}}$  is not to be confused with the contact stress vector  $\mathbf{t}$  and its components. When referring to the normal stress components of the interface, the diagonal values of  $\sigma^{\text{interface}}$  are meant. Normal contact stress refers to  $t_N$ .
- <sup>4</sup> Hourglass deformation modes are suppressed due to the Dirichlet boundary conditions.
- <sup>5</sup> Note that in the literature an averaging of the normal/tangential vectors of the two faces of the linearly interpolated finite-elements is conventionally performed.<sup>72,73</sup>

## REFERENCES

1. Lehane BM, Jardine R, Bond AJ, Frank R. Mechanisms of shaft friction in sand from instrumented pile tests. *J Geotech Eng.* 1993;119(1):19–35. [https://doi.org/10.1061/\(ASCE\)0733-9410\(1993\)119:1\(19\)](https://doi.org/10.1061/(ASCE)0733-9410(1993)119:1(19)).
2. Pincus HJ, Tabucanon J, Airey D, Poulos H. Pile skin friction in sands from constant normal stiffness tests. *Geotech Test J.* 1995;18(3):350–364. <http://doi.org/10.1520/GTJ11004J>.
3. Tsuha CHC, Foray PY, Jardine RJ, Yang ZX, Silva M, Rimoy S. Behaviour of displacement piles in sand under cyclic axial loading. *Soils Found.* 2012;52(3):393–410.
4. Jardine RJ, Standing JR. Field axial cyclic loading experiments on piles driven in sand. *Soils Found.* 2012;52(4):723–736. <http://doi.org/10.1016/j.sandf.2012.07.012>.
5. Salgado R, Loukidis D, Abou-Jaoude G, Zhang Y. The role of soil stiffness non-linearity in 1D pile driving simulations. *Géotechnique.* 2015;65(3):169–187. <http://doi.org/10.1680/geot.13.P.124>
6. Stutz HH, Wuttke F. Hypoplastic modeling of soil-structure interfaces in offshore applications. *J Zhejiang Univ Sci A.* 2018;19(8):624–637. <http://doi.org/10.1631/jzus.A1700469>.
7. Shahrour I, Rezaie F. An elastoplastic constitutive relation for the soil-structure interface under cyclic loading. *Comput Geotech.* 1997;21(1):21–39. [http://doi.org/10.1016/S0266-352X\(97\)00001-3](http://doi.org/10.1016/S0266-352X(97)00001-3)
8. Mortara G, Boulon M, Ghionna VN. A 2-D constitutive model for cyclic interface behaviour. *Int J Numer Anal Methods Geomech.* 2002;26(11):1071–1096. <http://doi.org/10.1002/nag.236>
9. Ghionna VN, Mortara G. An elastoplastic model for sand-structure interface behaviour. *Geotechnique.* 2002;52(1):41–50. <http://doi.org/10.1680/geot.2002.52.1.41>
10. Hu L, Pu J. Testing and modeling of soil-structure interface. *J Geotech Geoenviron Eng.* 2004;130(8):851–860. [http://doi.org/10.1061/\(asce\)1090-0241\(2004\)130:8\(851\)](http://doi.org/10.1061/(asce)1090-0241(2004)130:8(851))
11. Lashkari A. A plasticity model for sand-structure interfaces. *J Cent South Univ Technol.* 2012;19(4):1098–1108. <http://doi.org/10.1007/s11771-012-1115-1>
12. Liu J, Zou D, Kong X. A three-dimensional state-dependent model of soil-structure interface for monotonic and cyclic loadings. *Comput Geotech.* 2014;61:166–177. <http://doi.org/10.1016/j.compgeo.2014.05.012>
13. Saberi M, Annan CD, Konrad JM, Lashkari A. A critical state two-surface plasticity model for gravelly soil-structure interfaces under monotonic and cyclic loading. *Comput Geotech.* 2016;80:71–82. <http://doi.org/10.1016/j.compgeo.2016.06.011>

14. Saberi M, Annan CD, Konrad JM. Implementation of a soil-structure interface constitutive model for application in geo-structures. *Soil Dyn Earthq Eng*. 2019;116:714–731. <https://doi.org/10.1016/j.soildyn.2018.11.001>
15. Saberi M, Annan CD, Konrad JM. Three-dimensional constitutive model for cyclic behavior of soil-structure interfaces. *Soil Dyn Earthq Eng*. 2020;134:106162. <http://doi.org/10.1016/j.soildyn.2020.106162>
16. Yang J, Yin ZY. Soil-structure interface modeling with the nonlinear incremental approach. *Int J Numer Anal Methods Geomech*. 2021;45(10):1381–1404. <http://doi.org/10.1002/nag.3206>
17. Pang L, Jiang C, Ding X, Chen H, Deng L. A parameter calibration method in two-surface elastoplastic model for sand-structure interface under monotonic shear loading. *Comput Geotech*. 2021;134:104115. <https://doi.org/10.1016/j.compgeo.2021.104115>
18. Liu J, Zou D, Kong X. A two-mechanism soil-structure interface model for three-dimensional cyclic loading. *Int J Numer Anal Methods Geomech*. 2020;44(15):2042–2069. <https://doi.org/10.1002/nag.3118>
19. Liu W, Tian Y, Cassidy MJ. An interface to numerically model undrained soil-structure interactions. *Comput Geotech*. 2021;138:104327. <http://doi.org/10.1016/j.compgeo.2021.104327>
20. Gutjahr S. *Optimierte Berechnung von nicht gestützten Baugrubenwänden in Sand*. PhD thesis. Universität Dortmund; 2003.
21. Arnold M Application of the Intergranular Strain Concept to the Hypoplastic Modelling of Non-Adhesive Interfaces. Goa: 1. Conference IACMAG, 1-6 October; 2008.
22. Weißenfels C, Wriggers P. Methods to project plasticity models onto the contact surface applied to soil structure interactions. *Comput Geotech*. 2015;65:187–198. <https://doi.org/10.1016/j.compgeo.2014.11.015>
23. Stutz H, Mašin D, Wuttke F. Enhancement of a hypoplastic model for granular soil-structure interface behaviour. *Acta Geotech*. 2016;11(6):1249–1261. <http://doi.org/10.1007/s11440-016-0440-1>
24. Stutz H, Mašin D. Hypoplastic interface models for fine-grained soils. *Int J Numer Anal Methods Geomech*. 2017;41(2):284–303. <http://doi.org/10.1002/nag.2561>
25. Stutz H, Mašin D, Sattari AS, Wuttke F. A general approach to model interfaces using existing soil constitutive models application to hypoplasticity. *Comput Geotech*. 2017;87:115–127. <http://doi.org/10.1016/j.compgeo.2017.02.010>
26. Stutz H. *Hypoplastic Models for Soil-Structure Interfaces: Modelling and Implementation*. PhD thesis. Faculty of Mathematics and Natural Sciences at Kiel University; 2016.
27. Weißenfels C, Harish AB, Wriggers P. *Strategies to Apply Soil Models Directly as Friction Laws in Soil Structure Interactions*: Cham: Springer International Publishing; 2017:216–236.
28. Arnold M, Herle I. Hypoplastic description of the frictional behaviour of contacts. In: Schweiger H., ed. *Proceedings of the 6th European Conference on Numerical Methods in Geotechnical Engineering - Numerical Methods in Geotechnical Engineering*; 2006:101–106.
29. von Wolffersdorff PA. A hypoplastic relation for granular materials with a predefined limit state surface. *Mech Cohesive Frict Mater*. 1996;1:251–271.
30. Niemunis A, Herle I. Hypoplastic model for cohesionless soils with elastic strain range. *Mech Cohesive Frict Mater*. 1997;2(4):279–299. [https://doi.org/10.1002/\(SICI\)1099-1484\(199710\)2:4<279::AID-CFM29>3.0.CO;2-8](https://doi.org/10.1002/(SICI)1099-1484(199710)2:4<279::AID-CFM29>3.0.CO;2-8)
31. Dafalias YF, Manzari MT. Simple plasticity sand model accounting for fabric change effects. *J Eng Mech*. 2004;130(6):622–634. [http://doi.org/10.1061/\(asce\)0733-9399\(2004\)130:6\(622\)](http://doi.org/10.1061/(asce)0733-9399(2004)130:6(622))
32. Fischer KA, Wriggers P. Frictionless 2D contact formulations for finite deformations based on the mortar method. *Comput Mech*. 2005;36(3):226–244. <http://doi.org/10.1007/s00466-005-0660-y>
33. Fischer KA, Wriggers P. Mortar based frictional contact formulation for higher order interpolations using the moving friction cone. *Comput Methods Appl Mech Eng*. 2006;195(37-40):5020–5036. <http://doi.org/10.1016/j.cma.2005.09.025>
34. Tur M, Fuenmayor FJ, Wriggers P. A mortar-based frictional contact formulation for large deformations using Lagrange multipliers. *Comput Methods Appl Mech Eng*. 2009;198(37):2860–2873. <https://doi.org/10.1016/j.cma.2009.04.007>
35. Machaček J, Staubach P. numgeo: A finite-element program for the simulation of hydro-mechanically coupled geotechnical processes. *Fachsektionstage Geotechnik* 2021. DGGT, 2021. <https://dggt.de/images/PDF-Dokumente/bm-10s.pdf>
36. Machaček J Contributions to the Numerical Modelling of Saturated and Unsaturated Soils. Dissertation, Institute of Soil Mechanics and Rock Mechanics, Karlsruhe Institute of Technology, Issue No. 187; 2020.
37. Machaček J, Staubach P, Tafili M, Zachert H, Wichtmann T. Investigation of three sophisticated constitutive soil models: from numerical formulations to element tests and the analysis of vibratory pile driving tests. *Comput Geotech*. 2021;138:104276. <http://doi.org/10.1016/j.compgeo.2021.104276>
38. Staubach P, Machaček J, Sharif R, Wichtmann T. Back-analysis of model tests on piles in sand subjected to long-term lateral cyclic loading: Impact of the pile installation and application of the HCA model. *Comput Geotech*. 2021;134:104018. <http://doi.org/10.1016/j.compgeo.2021.104018>
39. Staubach P, Machaček J, Tafili M, Wichtmann T. A high-cycle accumulation model for clay and its application to monopile foundations. *Acta Geotech*. 2022. <http://doi.org/10.1007/s11440-021-01446-9>
40. Staubach P, Machaček J, Wichtmann T. Large-deformation analysis of pile installation with subsequent lateral loading: Sanisand vs. hypoplasticity. *Soil Dyn Earthq Eng*. 2021;151:106964. <http://doi.org/10.1016/j.soildyn.2021.106964>
41. Staubach P, Machaček J, Skowronek J, Wichtmann T. Vibratory pile driving in water-saturated sand: back-analysis of model tests using a hydro-mechanically coupled CEL method. *Soils Found*. 2021;61(1):144–159. <http://doi.org/10.1016/j.sandf.2020.11.005>
42. Staubach P, Machaček J, Tschirschy L, Wichtmann T. Enhancement of a high-cycle accumulation model by an adaptive strain amplitude and its application to monopile foundations. *Int J Numer Anal Methods Geomech*. 2022;46(2):315–338. <http://doi.org/10.1002/nag.3301>

43. Vogelsang J. *Untersuchungen zu den Mechanismen der Pfahlrammung*. PhD thesis. Veröffentlichung des Instituts für Bodenmechanik und Felsmechanik am Karlsruher Institut für Technologie (KIT), Heft 182; 2016.
44. Saberi M, Annan CD, Konrad JM. On the mechanics and modeling of interfaces between granular soils and structural materials. *Arch Civ Mech Eng*. 2018;18(4):1562–1579. <http://doi.org/10.1016/j.acme.2018.06.003>
45. Fakharian K, Evgin E. Cyclic simple-shear behavior of sand-steel interfaces under constant normal stiffness condition. *J Geotech Geoenviron Eng*. 1997;123(12):1096–1105. [http://doi.org/10.1061/\(asce\)1090-0241\(1997\)123:12\(1096\)](http://doi.org/10.1061/(asce)1090-0241(1997)123:12(1096))
46. Dumitrescu AI, Corfdir A, Frank R. Influence of the anisotropy of confining stress on the sand/steel interface behaviour in a cylinder shear apparatus. *Soils Found*. 2009;49(2):167–174. <https://doi.org/10.3208/sandf.49.167>
47. Martinez A, Frost JD, Hebler GL. Experimental study of shear zones formed at sand/steel interfaces in axial and torsional axisymmetric tests. *Geotech Test J*. 2015;38(4):409–426. <http://doi.org/10.1520/GTJ20140266>
48. Nardelli A, Cacciari PP, Futai MM. Sand-concrete interface response: the role of surface texture and confinement conditions. *Soils Found*. 2019;59(6):1675–1694. <https://doi.org/10.1016/j.sandf.2019.05.013>
49. Farhadi B, Lashkari A. Influence of soil inherent anisotropy on behavior of crushed sand-steel interfaces. *Soils Found*. 2017;57(1):111–125. <https://doi.org/10.1016/j.sandf.2017.01.008>
50. Fakharian K. *Three Dimensional Monotonic and Cyclic Behaviour of sand-steel interfaces: Testing and Modeling*. PhD thesis. University of Ottawa; 1996.
51. Zhang G, Zhang JM. Unified modeling of monotonic and cyclic behavior of interface between structure and gravelly soil. *Soils Found*. 2008;48(2):231–245.
52. Zhang G, Zhang JM. Large-scale monotonic and cyclic tests of interface between geotextile and gravelly soil. *Soils Found*. 2009;49(1):75–84. <http://doi.org/10.3208/sandf.49.75>
53. Feng DK, Zhang JM, Deng LJ. Three-dimensional monotonic and cyclic behavior of a gravel-steel interface from large-scale simple-shear tests. *Can Geotech J*. 2018;55(11):1657–1667. <http://doi.org/10.1139/cgj-2018-0065>
54. Zhang N, Evans TM. Three dimensional discrete element method simulations of interface shear. *Soils Found*. 2018;58(4):941–956. <https://doi.org/10.1016/j.sandf.2018.05.010>
55. Zhu HX, Zhou WH, Jing XY, Yin ZY. Observations on fabric evolution to a common micromechanical state at the soil-structure interface. *Int J Numer Anal Methods Geomech*. 2019;43(15):2449–2470. <https://doi.org/10.1002/nag.2989>
56. Huang M, Chen Y, Gu X. Discrete element modeling of soil-structure interface behavior under cyclic loading. *Comput Geotech*. 2019;107:14–24. <https://doi.org/10.1016/j.compgeo.2018.11.022>
57. Herle I, Nübel K. Hypoplastic description of the interface behaviour. In: Pande G, Pietruszczak S, Schweiger H., eds. *Numerical models in geomechanics. Proceedings of the 7th international symposium, Graz, September 1999*. 1999:53–58.
58. Vardoulakis I, Sulem J. *Bifurcation Analysis in Geomechanics*. CRC Press; 1995
59. Niemunis A. *Extended Hypoplastic Models for Soils*. Habilitation. Institute of Foundation Engineering and Soil Mechanics, Ruhr-University Bochum, Issue No. 34; 2003.
60. DeJong JT, White DJ, Randolph MF. Microscale observation and modeling of soil-structure interface behavior using particle image velocimetry. *Soils Found*. 2006;46(1):15–28. <http://doi.org/10.3208/sandf.46.15>
61. DeJong JT, Westgate ZJ. Role of initial state, material properties, and confinement condition on local and global soil-structure interface behavior. *J Geotech Geoenviron Eng*. 2009;135(11):1646–1660. [http://doi.org/10.1061/\(asce\)1090-0241\(2009\)135:11\(1646\)](http://doi.org/10.1061/(asce)1090-0241(2009)135:11(1646))
62. Mühlhaus HB, Vardoulakis I. The thickness of shear bands in granular materials. *Géotechnique*. 1987;37(3):271–283.
63. Dassault Systems Simulia. *Abaqus 6.14 theory guide*. 2014.
64. Kishida H, Uesugi M. Tests of the interface between sand and steel in the simple shear apparatus. *Geotechnique*. 1987;37(1):45–52. <http://doi.org/10.1680/geot.1987.37.1.45>
65. Fellin W, Ostermann A. Consistent tangent operators for constitutive rate equations. *Int J Numer Anal Methods Geomech*. 2002;26(12):1213–1233. <http://doi.org/10.1002/nag.242>
66. Rebstock D. *Verspannung und Entspannung von Sand entlang von Baukörpern*. PhD thesis. Karlsruher Institut für Technologie (KIT); 2011
67. Vogelsang J, Huber G, Triantafyllidis T. A large-scale soil-structure interface testing device. *Geotech Test J, ASTM*. 2013;36(5):613–625.
68. Vogelsang J, Huber G, Triantafyllidis T, Bender. *Interpretation of vibratory pile penetration based on Digital Image Correlation*. Springer Int Publishing Switzerland. 2015:31–51.
69. Tejchman J, Niemunis A. FE-studies on shear localization in an anisotropic micro-polar hypoplastic granular material. *Granul Matter*. 2006;8(3-4):205–220. <http://doi.org/10.1007/s10035-006-0009-z>
70. Bauer E, Ebrahimiyan B. Investigations of granular specimen size effect in interface shear box test using a micro-polar continuum description. *Int J Numer Anal Methods Geomech*. 2021;45(17):2467–2489. <https://doi.org/10.1002/nag.3273>
71. Wriggers P. *Computational Contact Mechanics*. Springer Berlin Heidelberg; 2006.
72. Popp A, Gee MW, Wall WA. A finite deformation mortar contact formulation using a primal-dual active set strategy. *Int J Numer Methods Eng*. 2009;79(11):1354–1391. <http://doi.org/10.1002/nme.2614>
73. Yang B, Laursen TA, Meng X. Two dimensional mortar contact methods for large deformation frictional sliding. *Int J Numer Methods Eng*. 2005;62(9):1183–1225. <http://doi.org/10.1002/nme.1222>
74. Bathe KJ. *Finite Element Procedures*. Prentice Hall; 2006.
75. Staubach P, Macháček J, Wichtmann T. Mortar contact discretisation methods incorporating interface models based on Hypoplasticity and Sanisand: application to vibratory pile driving. *Computers and Geotechnics*. 2022;104677. <https://doi.org/10.1016/j.compgeo.2022.104677>

**How to cite this article:** Staubach P, Machaček J, Wichtmann T. Novel approach to apply existing constitutive soil models to the modelling of interfaces. *Int J Numer Anal Methods*. 2022;1–31. <https://doi.org/10.1002/nag.3344>

## APPENDIX A: CONTACT MECHANICS OPERATIONS AND MORTAR CONTACT DISCRETISATION

The basic features of the mechanical description of the contact problem are given in the following. This includes the contact discretisation and the enforcement of the contact constraints. Since both are directly linked with the constitutive interface model, and they have been implemented in the finite-element code `numgeo`, a detailed description of the employed techniques is given in the following.

The contact pair has to satisfy the following conditions:

- Only contact pressure is possible:  $t_N \leq 0$
- A penetration is not allowed:  $g_N \geq 0$
- If the surfaces are not in contact, the contact stress is zero. If the gap is zero, the stress is unequal zero. These so-called *complementary conditions* are expressed by  $g_N t_N = 0$

The three conditions are also known as the *Karush-Kuhn-Tucker* (KKT) conditions. The contact conditions are interpreted as constraints in mechanical terms. These constraints can represent a condition on the displacement of two contact points and prevent them from penetrating into each other. For the contact constraint enforcement, the *penalty regularisation* and the *Lagrange multiplier* method are common approaches. Other methods such as the so-called *direct elimination*, *perturbed Lagrange* formulation and the *augmented Lagrange* method exist but are not considered in this work. For an overview over contact enforcement techniques and their advantages and disadvantages the interested reader is referred to Ref. 71. The penalty regularisation is used to enforce the normal contact constraints in the present work. The isoparametric description is used for the interpolation of the coordinates of the finite-element. The global coordinate is calculated using

$$\mathbf{x}(\xi) = \sum_I N_I(\xi) \mathbf{x}_I, \quad (\text{A1})$$

where the interpolation function  $N_I(\xi)$  at node  $I$  and the local coordinate  $\xi$  is used.  $\mathbf{x}(\xi)$  is the global coordinate at the local coordinate  $\xi$  of the element and  $\mathbf{x}_I$  is the global coordinate of node  $I$ . The interpolation function  $N_I$  is 1 at node  $I$  and zero at all other nodes. The number of components of  $\xi$  is identical to the number of dimensions and the local coordinate has the components  $\xi = [\xi, \eta, \zeta]^T$  for three-dimensional analyses.  $\xi$  and  $\eta$  are also employed as the local coordinate of element edges and faces, respectively. Where possible, the scalar components of the local coordinate are used in the following.

The derivation of the global coordinates with respect to the local coordinates is

$$\mathbf{x}_{,\xi}(\xi) = \sum_I \frac{dN_I(\xi)}{d\xi} \mathbf{x}_I, \quad (\text{A2})$$

which is also known as the element Jacobian  $\mathbf{J}^{\text{elem}}$ . The normal vector  $\mathbf{n}(\xi)$  at the edge of an element is given for 2D by

$$\mathbf{n}(\xi) = \frac{\mathbf{x}_{,\xi}(\xi) \times \boldsymbol{\tau}_3}{\|\mathbf{x}_{,\xi}(\xi)\|}, \quad (\text{A3})$$

where  $\boldsymbol{\tau}_3$  is defined by  $[0, 0, 1]^T$  and  $\mathbf{x}_{,\xi}(\xi)$  is the derivative of the global coordinate with respect to the local coordinate  $\xi$  evaluated at position  $\xi$  (only relevant for interpolation with order two or higher).  $\times$  marks the cross product. For three-dimensional analyses, the normal vector is defined by

$$\mathbf{n}(\xi, \eta) = \frac{\mathbf{x}_{,\xi}(\xi, \eta) \times \mathbf{x}_{,\eta}(\xi, \eta)}{\|\mathbf{x}_{,\xi}(\xi, \eta) \times \mathbf{x}_{,\eta}(\xi, \eta)\|}. \quad (\text{A4})$$

The tangential vectors orientated in the local coordinate system are determined using

$$\boldsymbol{\tau}_1(\xi) = \frac{\mathbf{x}_{,\xi}(\xi)}{\|\mathbf{x}_{,\xi}(\xi)\|} \quad (\text{A5})$$

for 2D and

$$\boldsymbol{\tau}_1(\xi, \eta) = \frac{\mathbf{x}_{,\xi}(\xi, \eta)}{\|\mathbf{x}_{,\xi}(\xi, \eta)\|} \quad \text{and} \quad \boldsymbol{\tau}_2(\xi, \eta) = \frac{\mathbf{x}_{,\eta}(\xi, \eta)}{\|\mathbf{x}_{,\eta}(\xi, \eta)\|} \quad (\text{A6})$$

for the 3D case. The integration of a function  $f(x, y, z)$  over a volume  $\Omega$  is done numerically using the *Gauss-quadrature* given by

$$\int_{\Omega} f(x, y, z) d\Omega = \int_{-1}^1 \int_{-1}^1 \int_{-1}^1 f[x(\xi, \eta, \zeta), y(\xi, \eta, \zeta), z(\xi, \eta, \zeta)] J^{\text{elem}}(\xi, \eta, \zeta) d\xi d\eta d\zeta \quad (\text{A7})$$

$$= \sum_{k=1}^{n_{\text{igp}}} \sum_{j=1}^{n_{\text{igp}}} \sum_{l=1}^{n_{\text{igp}}} f[x(\xi_k, \eta_j, \zeta_l), y(\xi_k, \eta_j, \zeta_l), z(\xi_k, \eta_j, \zeta_l)] J^{\text{elem}}(\xi_k, \eta_j, \zeta_l) w_k w_j w_l, \quad (\text{A8})$$

where the determinant  $J^{\text{elem}}$  of the element Jacobian  $\mathbf{J}^{\text{elem}}$  introduced in Equation (A2) is used.  $w_k$  is the weight of the integration point  $k$  and  $n_{\text{igp}}$  is the total number of integration points.

The minimum distance between the master and the slave surface is calculated using the *convective coordinate*  $\bar{\xi}$  (taking values from -1 to 1) along the master surface, which is illustrated in Figure A1. An orthogonal projection of the coordinates  $\mathbf{x}_I^{(1)}$  of slave node  $I$  onto the master surface  $\Gamma_c^{(2)}$  is performed for this purpose. This is done by enforcing the tangential vector of the master surface  $\mathbf{x}_{,\bar{\xi}}^{(2)}(\bar{\xi}^{(2)})$  to be orthogonal to the normal gap vector with minimum magnitude between the master surface and slave node  $I$ . The projection is defined by

$$\left[ \sum_J^{n_{\text{node}}} N_J^{(2)}(\bar{\xi}^{(2)}) \mathbf{x}_J^{(2)} - \mathbf{x}_I^{(1)} \right] \cdot \mathbf{x}_{,\bar{\xi}}^{(2)}(\bar{\xi}^{(2)}) = R \stackrel{!}{=} 0, \quad (\text{A9})$$

where the isoparametric description as introduced in Equation (A1) is used to calculate the coordinate of the master surface. To numerically find the solution of Equation (A9), Newton's method is applied. The required derivative of

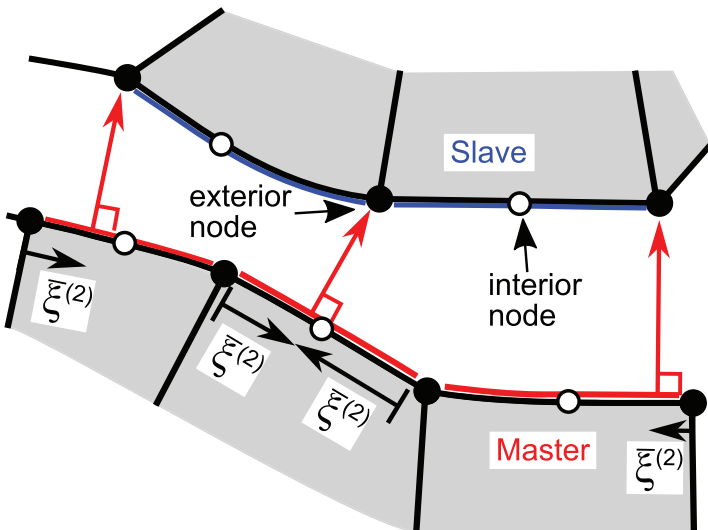


**FIGURE A1** Determination of the minimum distance between the paired surfaces using the convective coordinate  $\bar{\xi}$  along the master surface (only displayed for the exterior nodes)

Equation (A9) is given by

$$\begin{aligned} K &= \frac{\partial R}{\partial \xi} = \frac{\partial \mathbf{g}_I(\bar{\xi}^{(2)})}{\partial \xi} \cdot \mathbf{x}_{,\xi}^{(2)}(\bar{\xi}^{(2)}) + \mathbf{g}_I(\bar{\xi}^{(2)}) \cdot \mathbf{x}_{,\xi\xi}^{(2)}(\bar{\xi}^{(2)}) \\ &= \sum_J^{\text{nnode}} N_{J,\xi}(\bar{\xi}^{(2)}) \mathbf{x}_J^{(2)} \cdot \mathbf{x}_{,\xi}^{(2)}(\bar{\xi}^{(2)}) + \mathbf{g}_I(\bar{\xi}^{(2)}) \cdot \mathbf{x}_{,\xi\xi}^{(2)}(\bar{\xi}^{(2)}), \end{aligned} \quad (\text{A10})$$

with  $\mathbf{g}_I(\bar{\xi}^{(2)}) = [\sum_J^{\text{nnode}} N_J^{(2)}(\bar{\xi}^{(2)}) \mathbf{x}_J^{(2)} - \mathbf{x}_I^{(1)}]$ . The second term in Equation (A10) is only relevant for quadratically interpolated finite-elements since  $\mathbf{x}_{,\xi\xi}^{(2)}(\bar{\xi}^{(2)})$  is zero otherwise. Note that using quadratically interpolated finite-elements, a projection is performed for both *exterior* (located at the element corner) and *interior* (located at the element edge/on the element face) nodes.

Having satisfied Equation (A9) and  $\bar{\xi}^{(2)}$  obtained, the normal respectively tangential components of the distance of the slave node are calculated by

$$\mathbf{g}_{N,I}^{(1)} = \left[ \sum_J^{\text{nnode}} N_J^{(2)}(\bar{\xi}^{(2)}) \mathbf{x}_J^{(2)} - \mathbf{x}_I^{(1)} \right] \cdot \mathbf{n}^{(2)}(\bar{\xi}^{(2)}) \quad \text{and} \quad (\text{A11})$$

$$\mathbf{g}_{T,I,\alpha}^{(1)} = \left[ \sum_J^{\text{nnode}} N_J^{(2)}(\bar{\xi}^{(2)}) \mathbf{x}_J^{(2)} - \mathbf{x}_I^{(1)} \right] \cdot \left[ \boldsymbol{\tau}_\alpha^{(2)}(\bar{\xi}^{(2)}) \otimes \boldsymbol{\tau}_\alpha^{(2)}(\bar{\xi}^{(2)}) \right]. \quad (\text{A12})$$

$\mathbf{n}^{(2)}(\bar{\xi}^{(2)})$  is the normal vector of the master surface at the local coordinate  $\bar{\xi}^{(2)}$  and is defined by Equation (A4).  $\boldsymbol{\tau}_\alpha^{(2)}(\bar{\xi}^{(2)})$  is the tangential vector in direction  $\alpha = 1, 2$  (if the problem is three-dimensional) introduced in Equations (A5, A6). For frictional problems, the increment of the tangential gap  $\Delta \mathbf{g}_{T,\alpha}$  is required. It is calculated by

$$\Delta \mathbf{g}_{T,I,\alpha}^{(1)} = \left[ \sum_J^{\text{nnode}} N_J^{(2)}(\bar{\xi}^{(2)}) \Delta \mathbf{u}_J^{(2)} - \Delta \mathbf{u}_I^{(1)} \right] \cdot \left[ \boldsymbol{\tau}_\alpha^{(2)}(\bar{\xi}^{(2)}) \otimes \boldsymbol{\tau}_\alpha^{(2)}(\bar{\xi}^{(2)}) \right]. \quad (\text{A13})$$

$\mathbf{g}_{N,I}$  and  $\mathbf{g}_{T,I,\alpha}$  defined in Equations (A11, A12) determine the contact distance for node  $I$  of the slave surface. In order to determine the respective values for the master node  $J$ , the convective coordinate  $\bar{\xi}^{(1)}$  along the slave surface is computed, viz.

$$\left( \sum_I^{\text{nnode}} N_I^{(1)}(\bar{\xi}^{(1)}) \mathbf{x}_I^{(1)} - \mathbf{x}_J^{(2)} \right) \cdot \mathbf{x}_{,\xi}^{(1)}(\bar{\xi}^{(1)}) \stackrel{!}{=} 0. \quad (\text{A14})$$

The normal and tangential distances given by Equations (A11, A12) are then evaluated using  $\bar{\xi}^{(1)}$  to obtain  $\mathbf{g}_{N,J}^{(2)}$  and  $\mathbf{g}_{T,J}^{(2)}$ , defining the normal and tangential gap of the master node  $J$ .

For three-dimensional analyses, the convective coordinate has two components since the projection is performed on a face rather than a line. For the projection of the location of the slave node onto the face of the master surface, the convective coordinates  $\bar{\xi}^{(2)}$  and  $\bar{\eta}^{(2)}$  are evaluated by

$$\left( \sum_J^{\text{nnode}} N_J^{(2)}(\bar{\xi}^{(2)}, \bar{\eta}^{(2)}) \mathbf{x}_J^{(2)} - \mathbf{x}_I^{(1)} \right) \cdot \mathbf{x}_{,\xi}^{(2)}(\bar{\xi}^{(2)}, \bar{\eta}^{(2)}) \stackrel{!}{=} 0 \quad \text{and} \quad (\text{A15})$$

$$\left( \sum_J^{\text{nnode}} N_J^{(2)}(\bar{\xi}^{(2)}, \bar{\eta}^{(2)}) \mathbf{x}_J^{(2)} - \mathbf{x}_I^{(1)} \right) \cdot \mathbf{x}_{,\eta}^{(2)}(\bar{\xi}^{(2)}, \bar{\eta}^{(2)}) \stackrel{!}{=} 0. \quad (\text{A16})$$

Equations (A15, A16) are solved simultaneously using Newton's method. The required derivatives of Equations (A15, A16) in analogy to Equation (A10) build a  $2 \times 2$  matrix in this case. The local convective coordinates are updated every  $n$ -th

iteration by

$$\begin{bmatrix} \bar{\xi}^{(2)} \\ \bar{\eta}^{(2)} \end{bmatrix}_{n+1} = \begin{bmatrix} \bar{\xi}^{(2)} \\ \bar{\eta}^{(2)} \end{bmatrix}_n - \left[ \mathbf{g}_I(\bar{\xi}^{(2)}, \bar{\eta}^{(2)}) \cdot \mathbf{x}_{,\xi}^{(2)}(\bar{\xi}^{(2)}, \bar{\eta}^{(2)}) \quad \mathbf{g}_I(\bar{\xi}^{(2)}, \bar{\eta}^{(2)}) \cdot \mathbf{x}_{,\eta}^{(2)}(\bar{\xi}^{(2)}, \bar{\eta}^{(2)}) \right]_n \cdot \begin{bmatrix} \frac{\partial}{\partial \bar{\xi}^{(2)}} \left[ \mathbf{g}_I(\bar{\xi}^{(2)}, \bar{\eta}^{(2)}) \cdot \mathbf{x}_{,\xi}^{(2)}(\bar{\xi}^{(2)}, \bar{\eta}^{(2)}) \right] & \frac{\partial}{\partial \bar{\xi}^{(2)}} \left[ \mathbf{g}_I(\bar{\xi}^{(2)}, \bar{\eta}^{(2)}) \cdot \mathbf{x}_{,\eta}^{(2)}(\bar{\xi}^{(2)}, \bar{\eta}^{(2)}) \right] \\ \frac{\partial}{\partial \bar{\eta}^{(2)}} \left[ \mathbf{g}_I(\bar{\xi}^{(2)}, \bar{\eta}^{(2)}) \cdot \mathbf{x}_{,\xi}^{(2)}(\bar{\xi}^{(2)}, \bar{\eta}^{(2)}) \right] & \frac{\partial}{\partial \bar{\eta}^{(2)}} \left[ \mathbf{g}_I(\bar{\xi}^{(2)}, \bar{\eta}^{(2)}) \cdot \mathbf{x}_{,\eta}^{(2)}(\bar{\xi}^{(2)}, \bar{\eta}^{(2)}) \right] \end{bmatrix}_n^{-1}. \quad (\text{A17})$$

In analogy to the mortar method for 2D analyses, the projection is also performed on the faces of the finite-elements of the slave surface to evaluate the minimum distances of the master node. Hence, the equations

$$\left( \sum_I^{\text{nnode}} N_I^{(1)}(\bar{\xi}^{(1)}, \bar{\eta}^{(1)}) \mathbf{x}_I^{(1)} - \mathbf{x}_J^{(2)} \right) \cdot \mathbf{x}_{,\xi}^{(1)}(\bar{\xi}^{(2)}, \bar{\eta}^{(2)}) \stackrel{!}{=} 0 \quad \text{and} \quad (\text{A18})$$

$$\left( \sum_I^{\text{nnode}} N_I^{(1)}(\bar{\xi}^{(1)}, \bar{\eta}^{(1)}) \mathbf{x}_I^{(1)} - \mathbf{x}_J^{(2)} \right) \cdot \mathbf{x}_{,\eta}^{(1)}(\bar{\xi}^{(2)}, \bar{\eta}^{(2)}) \stackrel{!}{=} 0 \quad (\text{A19})$$

are solved iteratively.

The evaluation of the convective coordinates for 3D analyses is schematically shown in Figure A2. The grey element face indicates the slave surface for which the local convective coordinates are evaluated solving Equations (A18, A19) simultaneously using Newton's method. The convective coordinates are exemplary evaluated for 3 nodes of the master surface.

During the minimisation of Equations (A15 - A19) the local coordinates may exceed the boundaries of the element ( $\{\|\bar{\xi}\|, \|\bar{\eta}\|\} > 1$ ). In this case, the minimisation has to continue with the face of the next element to which the local coordinates point. Different cases have to be distinguished when evaluating the element face for which the projection continues depending on the value of the local coordinates and the local node label of the current element. If the convective coordinates reach a "natural" border, that is, the coordinates are spatially outside the defined surface zone, the mechanism stops.

The normal contact distance and increment in relative tangential movement are determined at the surface nodes. For the integration of the resulting contact stress, an interpolation to the integration points of the surface is made. Alternatively, the evaluation of the convective coordinates may be directly done for the coordinates of the integration points of the surface.  $\mathbf{x}_I^{(1)}$  in Equations (A15, A16) and  $\mathbf{x}_J^{(2)}$  in Equations (A18, A19) are replaced by  $\sum_I^{\text{nnode}} N_I^{(1)}(\xi_{\text{igp}}^{(1)}, \eta_{\text{igp}}^{(1)}) \mathbf{x}_I^{(1)}$  and

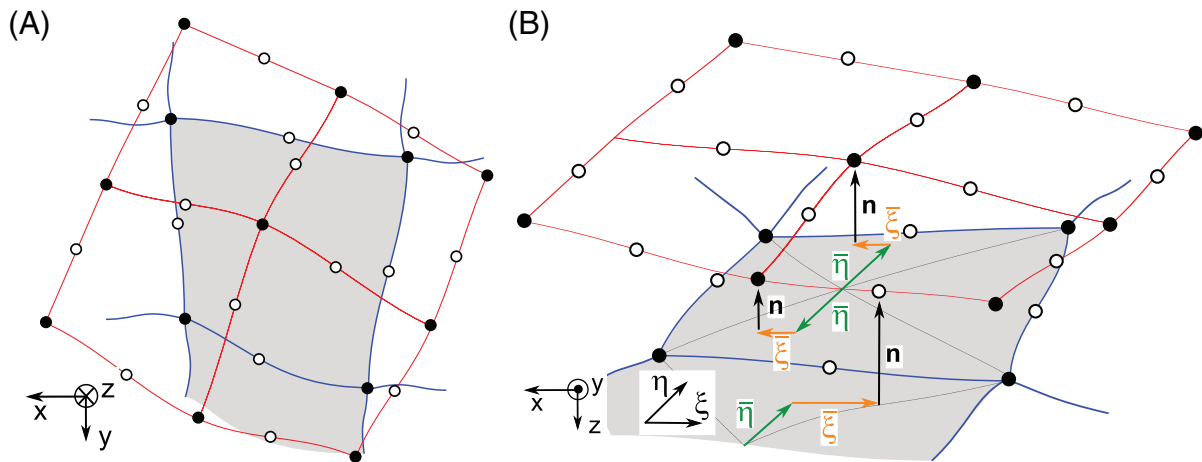


FIGURE A2 Evaluation of the convective coordinates of the slave surface for 3D analyses. (A) Shows the top-view on the surfaces. The exemplary evaluation of the convective coordinates of the slave surface by projection to three master nodes is given in (B)

$\sum_J^{\text{node}} N_J^{(2)}(\xi_{\text{igp}}^{(2)}, \eta_{\text{igp}}^{(2)}) \mathbf{x}_J^{(2)}$  in this case. An interpolation of the contact variables is not necessary using this approach. Both techniques are implemented in numgeo.

Using elements with linear interpolation, the surface geometry is a non-differentiable function leading to problems using the projection mechanism described in Equations (A15 - A19) when kinks between faces of different finite-elements exist. In case the local convective coordinates reach beyond the element border, the local tangential vector may jump. This can cause non-convergence of the projection algorithm and a wrong determination of the local convective coordinates. To prevent this, the change of the global coordinate with respect to the local coordinate  $\mathbf{x}_{,\xi}$  is determined using quadratic interpolation functions even if linearly interpolated finite-elements are used. The coordinates of the additional nodes for the quadratic interpolation are obtained by interpolation using the linear shape functions of the actual element. Using this approach,  $\mathbf{x}_{,\xi}$  is a smooth function and the convergence of Equations (A15 - A19) is secured<sup>5</sup>.

The normal contact contribution to the force equilibrium using the mortar discretisation technique is given by

$$\mathbf{r}_{N,I}^{(i)} = \sum_{\text{igp}}^{\text{ngp}} N_I^{(i)}(\xi_{\text{igp}}^{(i)}) t_{N,\text{igp}}^{(i)} \mathbf{n}_{\text{igp}}^{(i)} w_{\text{igp}}^{(i)} j_{\text{igp}}^{(i)} \quad \text{for } i = \{1, 2\}, \quad (\text{A20})$$

if the contact stress is directly evaluated at the integration points of the finite-element edge or face. The normal contact stress  $t_{N,\text{igp}}^{(i)}$  is calculated by multiplying the normal distance with the penalty factor.

For three-dimensional analyses, the contribution to the force equilibrium of the frictional contact forces  $\mathbf{r}_{T,I}^{(i)}$  is calculated using

$$\mathbf{r}_{T,I}^{(i)} = \sum_{\alpha}^{\text{ndim}-1} \sum_{\text{igp}}^{\text{ngp}} N_I^{(i)}(\xi_{\text{igp}}^{(i)}) t_{T,\text{igp},\alpha}^{(i)} \boldsymbol{\tau}_{\text{igp},\alpha}^{(i)} w_{\text{igp}}^{(i)} j_{\text{igp}}^{(i)} \quad \text{for } i = \{1, 2\}. \quad (\text{A21})$$

The calculation of the tangential contact stress components  $t_{T,\text{igp},\alpha}^{(i)}$  is subject of the main body of the paper. As elaborated on in Section 4, a numerical differentiation scheme is used to evaluate the required derivatives of Equations (A20, A21) with respect to the node displacement for an implicit solving scheme.

## APPENDIX B: CONVERGENCE RATE USING NUMERICAL DIFFERENTIATION VERSUS ANALYTICAL DERIVATIVES

To assess the superior convergence rate obtained using numerical differentiation compared to analytical derivatives of the hypoplastic interface model, the change of the norm of residual energy (for definition see Ref. 74) with respect to the number of iterations is given in Figure B1 for the simulation of the monotonic simple interface shear test (see Section 5). In case of the numerical differentiation scheme both approaches, the simplified Equation (37) where only the displacement increment is perturbed, and Equations (39, 40), for which in addition all state variables are also perturbed, are used. The first increment of the monotonic shearing phase of the simulation is considered. Note that the analytical derivatives of the hypoplastic model are not consistent, since an analytical calculation is not possible using the hypoplastic model

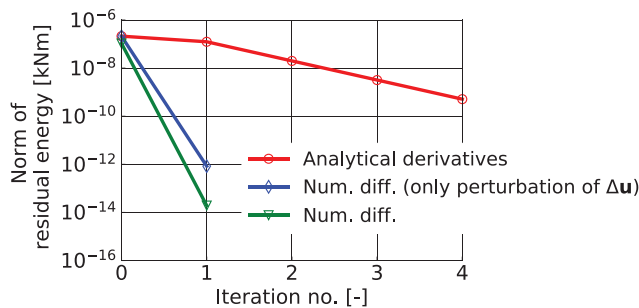


**FIGURE B1** Change of the norm of residual energy with respect to the number of iterations for the simulation of the monotonic simple shear test using either analytical derivatives for the Jacobian of the hypoplastic interface model or the numerical differentiation schemes. For the numerical differentiation either only  $\Delta \mathbf{u}$  is perturbed (according to Equation (37)) or all variables influencing the contact contributions (i.e., stress and other state variables according to Equation (39)) are perturbed

considered here. A simplified analytical derivative is calculated. In the following, the derivative used is shortly explained. The objective stress rate of the (continuum) hypoplastic model with intergranular strain extension is given by Ref. 30

$$\dot{\sigma} = \mathbf{M}(\boldsymbol{\sigma}, \mathbf{h}, e) : \dot{\boldsymbol{\varepsilon}}. \quad (\text{B1})$$

$\mathbf{M}$  is a fourth-order stiffness tensor,  $\mathbf{h}$  is the intergranular strain tensor and  $e$  the void ratio. Discretising in time using finite increments, the derivative of Equation (B1) with respect to the strain increment is given by

$$\frac{\partial \Delta \sigma_{ij}}{\partial \Delta \varepsilon_{mn}} = M_{ijmn} + \frac{\partial M_{ijkl}}{\partial \Delta \sigma_{kl}} \frac{\partial \Delta \sigma_{kl}}{\partial \Delta \varepsilon_{mn}} \Delta \varepsilon_{kl} + \frac{\partial M_{ijkl}}{\partial \Delta h_{kl}} \frac{\partial \Delta h_{kl}}{\partial \Delta \varepsilon_{mn}} \Delta \varepsilon_{kl} + \frac{\partial M_{ijkl}}{\partial \Delta e} \frac{\partial \Delta e}{\partial \Delta \varepsilon_{mn}} \Delta \varepsilon_{kl}. \quad (\text{B2})$$

Only the first term of Equation (B2) is considered. For the use as interface model, the derivative is then given in Voigt notation by

$$J_{ik}^{\text{interface}} = \frac{\partial \Delta \sigma_i}{\partial \Delta \varepsilon_j} \frac{\partial \Delta \varepsilon_j}{\partial \Delta g_k} = M_{ij} \frac{\partial \Delta \varepsilon_j}{\partial \Delta g_k}, \quad (\text{B3})$$

where  $\Delta g_k$  is the increment of relative surface movement (see Equation (A13) for the definition of the tangential part). Figure B1 shows that using the numerical differentiation schemes presented in Section 4, the residual energy decreases much more rapidly compared to the approach using the analytical derivative given by Equation (B3). Compared to the simplified differentiation scheme where only the displacement increment is perturbed, the complete numerical differentiation scheme gives a slightly better convergence rate. However, considering the much larger computational effort of the complete scheme as explained in Section 4, only the simplified scheme is used for the simulations presented in the main body.

### APPENDIX C: INFLUENCE OF THE INTERFACE MODELLING TECHNIQUE AND INITIALISATION OF INTERFACE STRESSES FOR THE SIMPLE INTERFACE SHEAR TESTS

The simulations of the monotonic simple interface shear test presented in Section 5 are repeated assuming perfectly rough conditions ( $\kappa = 1$ ) and are compared to a simulation without interface, using only the hypoplastic continuum model and prescribing the displacement of the steel plate to the nodes of the soil sample. This modelling approach without interface element only works for simulations with comparably small relative motions, since sliding can not be modelled without severe distortion of the continuum elements close to the interface zone (this aspect is important for the analysis of pile driving, for instance).

The results are given in Figure C1. Note that, as is also outlined in Section 5, the normal strains  $\varepsilon_{p1}$  and  $\varepsilon_{p2}$  are zero using the novel interface formulation since the interface in-plane normal stress components develop identical to the corresponding continuum stress components. This is due to the boundary conditions of the simple interface shear test and not generally the case. For the approach by Stutz et al. two different cases for the initialisation of the normal stress components in the interface are studied. The stress components are either initialised according to the initial continuum stress ( $\sigma_{p1,0} = \sigma_{22,0}$  and  $\sigma_{p2,0} = \sigma_{33,0}$ ), which is directly possible using numgeo, or initialised to the value of initial normal contact stress ( $\sigma_{p1,0} = t_{N,0}$  and  $\sigma_{p2,0} = t_{N,0}$ ), which corresponds to the restriction when using Abaqus. In terms of shear stress versus tangential displacement all interface approaches give results similar to the simulation without interface. However, the approach by Stutz et al. setting  $\sigma_{p1,0} = t_{N,0}$  and  $\sigma_{p2,0} = t_{N,0}$  gives slightly higher values of shear stress. This is absent if the interface stress is initialised by the continuum stress. Very similar results for all stresses are obtained using the novel approach and the approach of Stutz et al. setting  $\sigma_{p1,0} = \sigma_{22,0}$  and  $\sigma_{p2,0} = \sigma_{33,0}$ . It is also well visible that using the approach of Stutz et al. setting  $\sigma_{p1,0} = \sigma_{22,0}$  and  $\sigma_{p2,0} = \sigma_{33,0}$  almost no jump between the interface and the continuum stress develops. This, however, is only the case for the simple interface shear test considered here, since the normal strain of the interface and of the continuum is almost identical. For more complicated BVPs, as considered in Section 6, when using the approach by Stutz et al., the interface stress develops in general differently to the adjacent continuum stress.

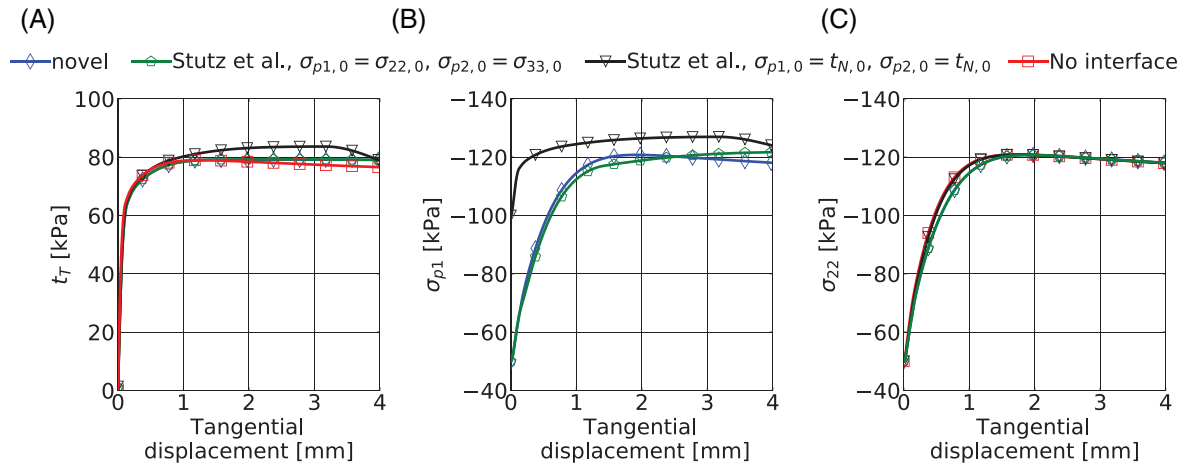


**FIGURE C1** Results of the simulation of a simple interface shear test with perfectly rough ( $\kappa = 1$ ) surface using the novel approach for the calculation of the stress conditions in the interface element, the approach by Stutz et al. with different initialisation of the normal stress components in the interface and an approach without interface zone. The interface shear stress and the interface normal stress component  $\sigma_{p1}$  versus the tangential displacement  $u_T$  of the steel plate are displayed in plot A) and B). In addition, the continuum normal stress component  $\sigma_{22}$  versus the tangential displacement is given in plot C). For the approach by Stutz et al. the initial stress components are either initialised according to the initial continuum stress ( $\sigma_{p1,0} = \sigma_{22,0}$  and  $\sigma_{p2,0} = \sigma_{33,0}$ ) or to the value of initial normal contact stress ( $\sigma_{p1,0} = t_{N,0}$  and  $\sigma_{p2,0} = t_{N,0}$ ). In case of the simulation without interface, the displacement of the steel plate is prescribed to the nodes of the soil sample, using only the hypoplastic continuum model